ARTICLE

New insights on the formation of the polymetamorphic Felbertal tungsten deposit (Austria, Eastern Alps) revealed by CL, EPMA, and LA-ICP-MS investigation

Cordula P. Haupt[1,3] · Joachim Krause[2] · Bernhard Schulz[3] · Jens Götze[3] · Johannes Chischi[3,4] · Jasper Berndt[1] · Stephan Klemme[1] · Steffen Schmidt[5] · Karsten Aupers[5,6] · Nils Reinhardt[5]

© The Author(s) 2024

Abstract

The Felbertal tungsten deposit is the only economic scheelite mine in Europe, yet its genesis is not fully understood. It has been argued recently that the formation of the deposit is most likely related to granitic intrusions of Variscan age, contrasting a previously suggested syn-depositional stratabound origin of Early Cambrian age. Solving this controversy remains challenging due to the polymetamorphic evolution of the deposit, which experienced both Variscan and Alpine metamorphism. In this contribution we present a comprehensive new data set of scheelite major, minor, and trace element concentrations from multiple scheelite generations of the Felbertal deposit along with microstructural observations. Our results show that Mo, Mo/Mn, REE, Y/Ho, Nb, and Nb/Ta in scheelite are variable within the different scheelite generations and are predominantly controlled by the host-rock lithologies on the local scale, whereas in general the data show a strong response to the shift of P, T, and pH upon changing magmatic-hydrothermal to metamorphic conditions. For the first time, we identify remnants of primary scheelite in the Western Ore Zone. The presented data support a magmatic-hydrothermal origin of the first scheelite mineralization during the Variscan orogeny with primary scheelite being characterized by wing-shaped REE patterns with a negative Eu-anomaly, high trace element concentrations, non-chondritic Y/Ho, and high Nb/Ta. Primary scheelite underwent metamorphic/hydrothermal alteration (recrystallization and dissolution-reprecipitation processes) during the Variscan and Alpine orogeny. This case study highlights that indicative mineralization-controlling geochemical ratios like Sr/Mn cannot be applied for polymetamorphic tungsten deposits like Felbertal.

✉ Cordula P. Haupt
chaupt1@uni-muenster.de

[1] Institut für Mineralogie, Universität Münster, Corrensstr. 24, 48149 Münster, Germany

[2] Helmholtz-Institut Freiberg für Ressourcentechnologie, Chemnitzer Str. 40, 09599 Freiberg, Germany

[3] Institut für Mineralogie, TU Bergakademie Freiberg, Brennhausgasse 14, 09599 Freiberg, Germany

[4] Murdoch University, 90 South Street, Murdoch Western Australia, Perth 6150, Australia

[5] WOLFRAM Bergbau und Hütten AG, St. Martin i. S., Austria

[6] Volkswagen AG, Berliner Ring 2, Wolfsburg, Germany

Introduction

Scheelite and wolframite group minerals are the most important carriers of tungsten (W) in economic W ore deposits. Most W is mined in China (USGS 2022), from granite-related vein and skarn-type deposits (Mao et al. 2019).

In Europe, scheelite-only deposits are rare. The largest active European scheelite mine, owned and operated by Wolfram Bergbau und Hütten AG (WBH), is the Felbertal tungsten mine in Mittersill, Austria (Fig. 1a). The deposit is unique, since its geological history is a complex combination of orogenic processes, which mobilized magmatic and metamorphic hydrothermal fluids generating the multistage Felbertal deposit (e.g., Schenk and Höll 1991; Eichhorn et al. 1995; Höll and Eichhorn 1998). The deposit is subdivided into an Eastern and a Western ore zone (Fig. 1b)
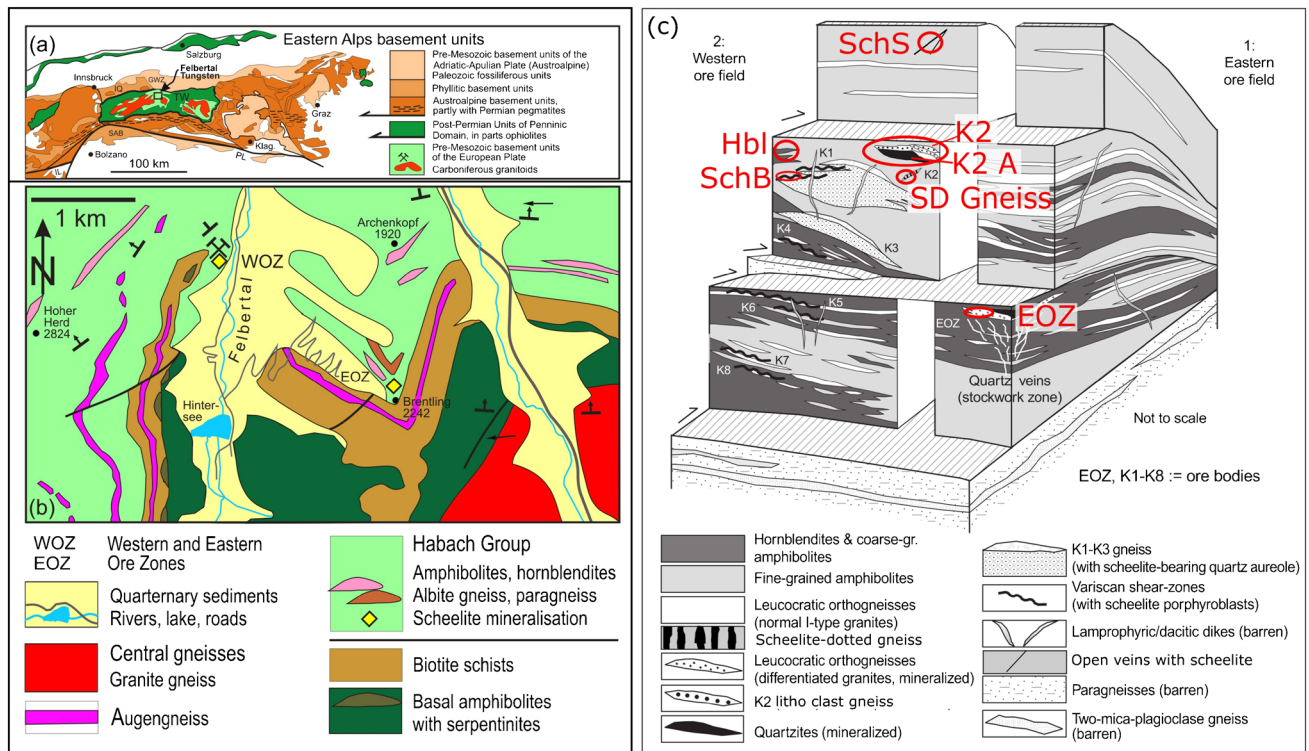
Fig. 1 (a) Basement units in the Eastern Alps and location of the Felbertal tungsten deposit in the Tauern Window (TW). GWZ Graywacke Zone; IQ Innsbruck Quartzphyllite; PL Periadriatic Lineament; SAB Southalpine basement. (b) Geological sketch with locations of the Eastern and Western Ore Zones (EOZ, WOZ) of the Felbertal tungsten deposit, modified after Kozlik et al. (2016a) (c) schematic block diagram modified after Eichhorn et al. (1999) of the EOZ and WOZ with lithologies and sampling areas of this study. Note that superposition is no age indicator, since the deposit experienced multiple stages of metamorphic overprint

abbreviated as EOZ and WOZ, respectively. The latter is currently mined as an underground operation. Ore bodies in the WOZ are distinguished as K1-K8 and SD-gneiss, according to macroscopic differences (e.g., host-rock, ore grade, style of mineralization; comp. Fig. 1c).

The Felbertal deposit does not unambiguously fit into one of the pre-defined categories (i.e., vein-type / skarn-related / intrusion-related), nor does its scheelite mineralization solely correspond to a magmatic, hydrothermal, or metamorphic type (Poulin et al. 2018). It has been discussed that the major and trace element composition of scheelite is sensitive to its host-rock, oxygen fugacity, salinity, co-genetic minerals, and the composition of the mineralizing fluids (e.g., Xiao et al. 2022; Miranda et al. 2022; Li et al. 2024), making it a promising tracer for exploration targeting. In the light of these findings, it remains to be tested how the Felbertal deposit fits into existing categories to classify the origin of scheelite-mineralizing fluids.

Based on structural and geochemical evidence, several multi-stage scheelite evolution models have been discussed controversially for the Felbertal deposit , (Höll et al. 1972; Höll 1975; Eichhorn et al. 1997; Raith and Stein 2006; Kozlik and Raith 2017). The first scheelite mineralization was originally postulated to be of syn-depositional-exhalative origin linked to Early Paleozoic volcanism, based on field observations predominantly made in the EOZ (Höll et al. 1972; Höll and Schenk 1988) and Sm-Nd isotope systematics (Eichhorn et al. 1997). However, these age determinations were highly speculative with associated uncertainties of > 100 Ma and the age of the first scheelite mineralization was subsequently revised based on investigations of one of the heavily mineralized ore bodies accessible in the WOZ ("K1-K3 orthogneiss"), a highly fractionated meta-granite of Variscan age (Kozlik and Raith 2017). Based on its trace element systematics, the first scheelite mineralization appears to be linked to the Variscan orogeny and successive magmatism in the Eastern Alps. Re-Os dating of scheelite-associated molybdenite confirms a Variscan age, yielding ages of around 340 Ma (Raith and Stein 2006). The primary scheelite was further overprinted by regional tectonic and metamorphic processes linked to the Variscan (360–320 Ma) and later Alpine orogeny (~80 Ma) (Eichhorn et al. 1995, 1997).

Geochemical indicators may be crucial to further distinguish different scheelite generations and the processes responsible for their formation: four generations (I–IV) are

currently distinguished. They could potentially help to get an idea on where the initial W originated from. If indeed there are trace elemental signatures which can additionally be used to classify scheelite mineralizing fluids in the Felbertal deposit, it needs to be shown how these compare with global datasets on scheelite (e.g., Sciuba et al. 2020; Miranda et al. 2022). Therefore, our study focuses on two well-mineralized ore bodies in the WOZ: The K2 ore body (gneiss-rich and amphibolite-rich domains) and an orthogneiss (SD-gneiss) containing disseminated scheelite. The latter forms a separate ore body that has no significance in the upper parts of the deposit but seems to become larger with depth (Fig. 1c). Here, we present a new dataset of trace elements in scheelite from the Felbertal tungsten deposit which contributes to the genetic interpretation of this unique deposit by combining microstructural investigations with major and trace element analysis of scheelite of different generations. We compare these data with one texturally typical sample of the EOZ (banded quartzite), considered to represent the first scheelite generation (Höll 1975; Eichhorn et al. 1997).

Geological setting of the Felbertal scheelite deposit

The Felbertal tungsten deposit is located in the Penninic Basement of the Tauern Window in the Eastern Alps (Schmid et al. 2013; Fig 1a). It is hosted by the Early Paleozoic Habach Complex (HC), whose predominantly mafic meta-volcanic rocks show the geochemical characteristics of a continental island arc (Fig. 1b). The HC and associated units were part of peri-Gondwana, which was deformed and metamorphosed during the Variscan Orogeny. Various Carboniferous and Early-Permian granitoids (360–270 Ma), also referred to as Variscan granitoids/Central Gneisses (*Zentralgneise;* Fig. 1b), intruded the Early-Paleozoic sequences (Raith et al. 2018). During the late Oligocene to Miocene, the units of the European Plate were thrusted beneath the remnants and cover of the Penninic oceanic crust (*Obere Schieferhülle/Glocknerdecke)*, and the southern Adriatic-Apulian Plate (*Austroalpine Nappe Unit)* (Schmid et al. 2013).

The HC is subdivided into a Lower and Upper Magmatic Series (LMS and UMS, respectively; Höck 1993), the former hosting the Felbertal tungsten deposit (Höll 1975). The predominant host rocks of the Felbertal deposit are meta-igneous rocks with minor amounts of meta-sedimentary rocks, such as banded and foliated amphibolites, as well as minor leucocratic granitoids (Höll 1975) of the HC (Fig. 1b). In the LMS, the protoliths are interpreted as tholeiitic MOR basalts. These units yield zircon U-Pb SHRIMP ages of between 547 ± 27 Ma for barren host-rocks and 519 ± 18 Ma for mineralized gneiss bodies of the K2 ore body. Overlapping ages of first isotope dating studies suggested that the younger age dated the formation of the first scheelite

(Eichhorn et al. 1997, 1999). Hornblendite and coarse-grained amphibolite in the LMS form up to several m thick sequences. By their bulk rock chemistry, they have been interpreted as boninitic volcanic arc magmas (Thalhammer 1987). The coarse-grained amphibolite likely represents metagabbros. A conventional U-Pb zircon age of 496 ± 2 Ma from a hornblendite was interpreted as the time of the magmatic emplacement (Von Quadt 1993).

Felbertal ore bodies

With the Lower Magmatic Series of the Habach Complex as the emplacement position of the Felbertal tungsten deposit (Höck 1993), intermediate to felsic orthogneisses occur as several m-thick intercalations throughout this complex. They are summarized as pre-Variscan orthogneisses (*Augengneiss* in Fig. 1b) and show chemical similarities with calc-alkaline I-type volcanic arc granites (Höll and Eichhorn 1998). The EOZ consists of a stockwork mineralization zone overlain by a massive laminated scheelite-quartzite ore (scheelite-rich quartzite), which is spatially associated with an orthogneiss body (*Ostfeldgneiss*), hornblendite, and amphibolite rocks. The EOZ was mined out in 1986 (Raith et al. 2018).

The ore bodies of the WOZ (K1–K8, SD gneiss) are distributed within two mineralized areas, namely K1–K4 and SD gneiss (upper wedge) and K5–K8 (lower wedge), which are separated by a barren basal schist wedge (Schmidt 1988). Economically important are the K1-K3 orthogneiss, K2 (hornblende schist and K2 *Breccia*), K4, K5 (both related to mainly hornblendite, Gneiss and coarse-grained amphibolite intercalation), K6 (structurally very similar to K2 *Breccia*), K7 (Qtz-veins cutting hornblende schist rocks), K8 (strongly mineralized quartz veins cutting through amphibolite and gneiss plus associated hornblendite) and the SD-gneiss ("scheelite-dotted" gneiss, an orthogneiss with mostly disseminated scheelite mineralization Raith et al. 2018).

Age of the mineralization according to host lithologies

Initially, the pre-Variscan gneisses present in the Tauern Window were interpreted as metavolcanic rocks but intrusive contacts support an intrusive origin for at least some of them. The leucocratic albite-muscovite gneiss (*Ostfeldgneiss*) underlying the foliated scheelite-quartz ores in the EOZ was dated at 529 ± 17 Ma (Eichhorn et al. 1999). Orthogneisses in the WOZ referred to as Older and Younger K2 gneiss are also of intrusive origin. These gneisses are associated with the metabreccia, referred to as "eruption breccia" in the first studies, which is nowadays interpreted as a tectonic breccia (Höll and Schenk 1988; Raith et al. 2018). Due to the omnipresence of ductile deformation, this unit represents a tectonic melange zone with elongated

clasts of different lithologies ranging from amphibolite to felsic gneiss in a gneiss matrix and is therefore referred to as lithoclast gneiss in this study. Gneiss clasts dated by U-Pb in zircons yield an age of 529 ± 18 Ma, identical to the Younger K2 gneiss unit (Eichhorn et al. 1999). Eichhorn et al. (1999) argued for a first mineralization stage of Cambrian age (≈520 Ma) and a second stage of Lower Carboniferous (≈340 Ma) tungsten mineralization. More recent *in-situ* U-Pb dating of scheelite relict cores from the foliated ores in the EOZ yielded an age of 335.5 ± 4.6 Ma (Raith et al. 2011) and match the 336–340 Ma zircon protolith ages of the K1-K3 orthogneiss (Eichhorn et al. 1999). These more recent ages allowed for a reinterpretation of the first scheelite precipitation, which seems to be tied to the intrusion of the Early Carboniferous K1-K3 orthogneiss bodies (e.g., Kozlik et al. 2016a; Kozlik and Raith 2017). These gneisses are highly evolved metaluminous to peraluminous magnesian monzogranites (Kozlik and Raith 2017), showing overlapping I- to A-type characteristics (Finger and Steyrer 1988). They have elevated concentrations of Rb, Cs, Nb, Ta, Be, Li, Bi, Sn, Cs, Th, F, U, Mo, and W and show REE patterns with LREE enrichment. The initial $^{87}Sr/^{86}Sr$ values range from 0.704 to 0.708 and the εNd values from –4 to –6 (Höll and Eichhorn 1998). The initial εHf values vary from −7.6 to −4.3 and indicate a Mid-Proterozoic continental crustal source (Kozlik et al. 2016b). The K1-K3 orthogneiss in the Felbertal mine and the associated holo-leucocratic aplitic gneiss are the most differentiated granitic melts (Kozlik and Raith 2017). Porphyritic, lamprophyric or dacitic dykes are important for constraining the relative timing of scheelite mineralization. They are barren and crosscut scheelite-bearing quartz veins, shear zones with scheelite, and the K1-K3 orthogneiss. If at all, they contain only remobilised scheelite formed during Alpine metamorphism (Schenk 1990). One of these dacitic dykes was dated at 340 ± 5 Ma (Eichhorn et al. 1999). This age overlaps within error with the U-Pb ages of the K1-K3 orthogneiss (Kozlik et al. 2016b), the Re-Os molybdenite ages (Raith and Stein 2006), and the U-Pb age of a scheelite sample from the EOZ (Raith et al. 2011).

A Sm-Nd isochron age of 319 ± 34 Ma (Eichhorn et al. 1997) for a late scheelite generation (Scheelite III, see below) at Felbertal was attributed to Variscan regional metamorphism and so were ages as young as 282 ± 2 Ma (U-Pb dating on titanite, Eichhorn et al. 1995). Re-Os ages of molybdenite associated with different scheelite generations range between ~358 and ~336 Ma and confirm multiple episodes of magmatic-hydrothermal and metamorphic mineralization related to the Variscan orogeny (Raith and Stein 2006). Pb-U-Th systematics in uranitites in metagranitoids from the Tauern Window revealed that there are Permian (265 Ma) and Triassic (~215 Ma) low-temperature thermal events that predate the medium-grade Alpine regional metamorphism, and formation of the Alpine veins (Finger et al.

2017). These findings add to a complex regional geologic context.

Scheelite generations

The ages inferred for the orthogneiss protolith of the tungsten mineralization, the emplacement of the barren dykes, and the Variscan regional metamorphism indicate that scheelite emplacement and first metamorphism occurred in a tightly constrained time interval of <10 Ma. However, the available age data are not precise enough to further resolve these events. The genetic complexity of the Felbertal tungsten deposit is also reflected in the four scheelite generations (I–IV) which have been distinguished (Höll 1975; Schenk et al. 1990; Eichhorn et al. 1997, 1999; Raith et al. 2011; Kozlik et al. 2016b; Kozlik and Raith 2017):

Scheelite I is characterized by yellowish-white luminescence in short-wave UV light (wavelength of scheelite fluorescence is 254 nm). Its MoO_3 concentration does not exceed 1.2 wt% and it is very fine-grained (<0.4 mm). Raith et al. (2011) and Kozlik et al. (2016a) reported a remarkable small-scale oscillatory growth zoning in cathodoluminescence (CL). According to these authors, scheelite I is exclusively present in the EOZ in association with scheelite-rich laminated scheelite-quartz ores (cf. Höll 1975; Schenk et al. 1990). A possible, yet unverified, equivalent could be seen in foliated scheelite-quartz ores in the K2 ore body of the WOZ (Raith et al. 2018).

Scheelite II is the most common scheelite stage in the WOZ. It is easily recognized according to its yellow fluorescent color in UV light and variable grain sizes of mm- to cm-scale. Molybdenum concentrations are reported to be similar to scheelite I (Eichhorn et al. 1997; Raith et al. 2018). Large scheelite II crystals show primary growth zoning, visualized in CL images. In high-strain zones, scheelite II is commonly observed to form porphyroclasts (Kozlik et al. 2016a), which are intergrown with recrystallized scheelite III along microfractures. Veins with quartz and scheelite II crosscut the K1-K3 orthogneiss, which underlines an Early Carboniferous maximum crystallization age (Raith et al. 2018).

Scheelite III has been reported in both the EOZ and WOZ. It is characterized by bluish luminescence color in UV light, low Mo concentrations and bright luminescence in CL. This scheelite generation is a recrystallization phenomenon of scheelite I and II (Kozlik et al. 2016a). It appears as rims around older scheelite and has also been described to fill micro-fractures within these earlier generations. Eichhorn et al. (1997) presented a Sm-Nd isochron age for scheelite III of 319 ± 34 Ma. According to their work, this age may represent the period of recrystallization of earlier scheelite generations during Variscan regional metamorphism. The bulk ore extracted from the WOZ is characterized as scheelite II and III.

Scheelite IV is characterized by white to pale-blue luminescence and is almost free of Mo. It is less common in the mine than II and III (Raith et al. 2018). Scheelite IV grains may reach cm-dm in size. They grow as pseudo octahedral idiomorphic crystals within Alpine quartz veins that crosscut older Variscan structures, including the first generation of quartz-scheelite veins. A Sm-Nd isochron yielded Alpine ages of 29 ± 17 Ma for scheelite IV, which is interpreted to reflect local remobilization of earlier scheelite generations during Alpine regional metamorphism (Eichhorn et al. 1997). This agrees with garnet-bulk rock Sm-Nd and Rb-Sr ages of 30 ± 1 Ma and 31 ± 5 Ma ages, respectively, of the K1-K3 orthogneiss which indicate a young Alpine metamorphic overprint (Eichhorn et al. 1997).

Methods

Sampling for this study

For this study, different types of scheelite mineralization and ore bodies were sampled (details given in the Electronic Supplementary Material - ESM Table 1). Scheelite is classified according to the existing characterization (Höll 1975; Schenk et al. 1990; Eichhorn et al. 1997, 1999; Raith et al. 2011; Kozlik et al. 2016b, a; Kozlik and Raith 2017). Samples were collected from mine levels between 880–625 m asl. They mainly originate from the K2 and the SD-gneiss ore body (Fig. 1c shows the ore bodies analyzed in this study; ESM Fig. 1–4)

A hornblendite schist sample from the K1-K3 ore body and one characteristic sample from the EOZ were included to cover a wider lithological range (ESM Table 1). The hornblende schist was provided from an internal collection. The sample of the EOZ (Sample ID: 136019, WBH collection), originates from the banded scheelite-quartzite ores (*Reicherz*) (ESM Fig. 4a–b, 5c).

Scheelite IV with bright blue luminescence was sampled individually from a late-stage quartz vein (ESM Fig. 4c, scheelite B which will be referred to as scheelite IVa). A second fragment of scheelite IV (scheelite S, further referred to as scheelite IVb) originates from a clear gem-quality scheelite (6–8 cm diameter) found in a late-stage open Alpine vein. It co-crystallized with chlorite, quartz, and albite at a depth of 1175 m asl. Its fluorescent color is white to pale blue (ESM Fig. 4d).

For comparison, two gneisses (orthogneiss sample 736-2 of the SD gneiss ore body and felsic sample K2 880BZ from the K2 lithoclast gneiss) were analyzed.

Analytical methods

Sample preparation (Iridium strip-heater)

Bulk rock and trace element analysis of selected samples (SD-gneiss samples and samples from the K2 ore body: referred to as lithoclast gneiss in this study) were performed using glass beads made with an iridium strip heater (Fedorowich et al. 1993; Stoll et al. 2008) at Institut für Mineralogie, Universität Münster, Germany. Samples were crushed and ground to powders at Helmholtz-Institute Freiberg for Resource Technology, Germany, using a Laarmann LMBM 2000 planetary ball mill loaded with agate crucibles and balls. Homogeneous glass beads of the resulting powder were prepared following the procedure described in Stoll et al. (2008). In order to validate precision and accuracy, triplicates for SD-gneiss 736-2 were produced. The glass beads were mounted on glass slides or prepared as polished epoxy mounts. Only well-homogenized samples were considered for further analysis.

Cathodoluminescence (CL)

Cathodoluminescence microscopy was performed on selected samples for qualitative description of scheelite zonation. Measurements were done on polished and carbon-coated thin sections using a "hot cathode" CL microscope HC1-LM (Neuser et al. 1995) at the Institut für Mineralogie, Technische Universität Bergakademie Freiberg, Germany. The excitation depth of the defocused electron beam is in the range of 2–8 µm. The system was operated at 14 kV accelerating voltage and a current of 0.01 mA (current density of about 0.5 µA/mm^2). Luminescence images were captured "on-line" during CL operations with a peltier cooled digital video-camera (OLYMPUS DP72) using Stream Start 1.7 software (Olympus Soft Imaging Solutions GmbH). CL spectra in the wavelength between 370 to 1000 nm were recorded with an Acton Research SP-2356 digital triple-grating spectrograph with a Princeton Spec-10 CCD detector that was attached to the CL microscope by a silica-glass fiber guide, using the corresponding WinSpec, Version 2.5 spectra software. Photos and spectra cannot be taken simultaneously. The CL spectra were measured under standardized conditions after wavelength calibration by a Hg-halogen lamp at a spot width of 30 µm and a measuring time of 1 s. Spectra were plotted and compared with data in Randall (1939), Mariano and King (1975), and Gaft et al. (1998, 2005). Raw data of the spectral CL measurements and images can be found in ESM CL and a typical spectrum can be seen in Fig. 4b.

Electron probe microanalysis (EPMA)

Quantitative element distribution maps of scheelite within host-rock samples using wavelength dispersive spectrometers (WDS) and quantitative analyses of scheelite were performed with a JEOL JXA 8530 F Hyperprobe at the Helmholtz Institute Freiberg for Resource Technology (HIF), Germany. An acceleration voltage of 20 kV, a probe current of 50 nA and a dwell time of 100 ms were chosen. Step sizes ranged from 11–31 μm. Beam diameter was always 1 μm smaller than the step-size.

The CL signal during the EPMA measurements was recorded with a panchromatic detector and converted to false color images. Back scattered electron images were recorded but appeared distorted due to the strong scheelite luminescence. Quantitative mineral-chemical analyses on scheelite by EPMA were performed along transects and on single spots using an acceleration voltage of 20 kV, a probe current of 100 nA and a defocused beam with a diameter between 2–10 μm. Step width was chosen according to the size of the analyzed scheelite and the required resolution. Measurements were carried out in an asynchronous mode using all five wavelength dispersive spectrometers. The glass beads of homogenized whole-rock samples were also analyzed at the EPMA in Freiberg (HIF) for major elements. Acceleration voltage was set to 20 kV and the probe current to 30 nA. The chosen beam diameter was 15 μm. Silicate minerals of two thin sections (K2 883-15-1, SD 625 Be2; ESM Table 1) were analyzed at the Institut für Mineralogie at Universität Münster, Germany with the JEOL JXA 8530 F Hyperprobe using an acceleration voltage of 15 kV, a probe current of 15 nA, and a beam diameter of 5 μm. Further details of the analytical protocols and the data reduction can be found in ESM Table B.

Laser ablation inductively coupled plasma mass spectrometry (LA-ICP-MS)

A total of 689 measurements on the scheelite samples was performed with LA-ICP-MS; this included 31 transects and individual grains, 11 measurements on silicates associated with scheelite, and 10 measurements of each homogenized host rock (ESM Table 1, ESM Table C). Scheelite analyses with a concentration of Si above 1000 μg/g were considered as mixed analyses with silicate phases and excluded from the dataset. Scheelites IVa and IVb were measured periodically as in-house reference materials because of their homogeneity.

The measurements were performed in the LA-ICP-MS laboratory at the Institut für Mineralogie at Universität Münster, Germany, which is equipped with a Teledyne Photon Machines Analyte G2 193 nm Excimer LASER ablation system working at 193 nm wavelength with a repetition rate of 10 Hz, coupled to a Thermo Scientific Element XR double focusing sector field mass spectrometer. The beam diameter was chosen to be between 40–60 μm. ^{43}Ca was used as an internal standard element for scheelite, ^{29}Si for silicate glasses and silicate minerals. NIST 612 glass was used as standard (Jochum et al. 2011). Reference materials BIR-1G, GSD-1G, and GSE-1G were analyzed every ~15 analyses as unknowns to assure accuracy and reproducibility of the measurements. Typical relative standard errors of the measured concentrations lie between 1–10 % for most elements. ^{88}Sr, ^{89}Y, ^{93}Nb, REE, ^{181}Ta, ^{182}W, ^{183}W and ^{208}Pb had errors between 1–5 %. Further analytical details can be found in ESM Table C and ESM Data reduction. Rare earth element concentrations and ratios were normalized to the chondritic values of McDonough and Sun (1995). The Eu-anomaly was calculated from the chondrite normalized element concentrations as Eu/[sqrt(Sm x Gd)](Ghaderi et al. 1999). Values below the lower limit of quantification are not shown in the diagrams. As a measure for the accuracy of the LA-ICP-MS analyses, there is an overall very good agreement of Mo concentrations determined by LA-ICP-MS and EPMA (ESM Fig. 8).

Results

Petrography and mineralogy

Analytical findings of all samples are summarized in ESM Table 1. Samples from the K2 ore body (lithoclast gneiss, ESM Fig. 1a–b and 3) originate from either gneiss-rich (K2 883-) or amphibole-rich domains (K2 880 BZ, K2 Amph-2), which were both sampled in the area described by Höll and Schenk (1988) as tectonic breccia (ESM Fig. 3a, b). The amphibole-rich lithoclasts are up to decimeters in size and they are embedded in a matrix of mostly felsic gneisses. Amphibole-rich and felsic domains are strongly sheared and co-axially stretched (ESM Fig. 1a, b). Scheelite occurs predominantly as generation II and III in the quartz-rich layers and in veins in gneiss-rich, to a minor extent, amphibole-rich domains. Amphibole-rich samples from the K2 ore body are strongly foliated and scheelite is mostly situated in thin quartz layers (ESM Fig. 3b).

The SD-gneiss (orthogneiss "a") mainly consists of albite, quartz, and minor amounts of amphibole. The mica concentration varies between 10–20 vol%, micas are aligned along foliation and lepidoblastic biotite underlines lithologic contacts. The mineralization style in the SD-gneiss is, in contrast to other ore bodies of the deposit, mostly disseminated (ESM Fig. 1c, d; Kozlik 2015; Raith et al. 2018). The SD-gneiss also contains cm to dm thick, deformed quartz veins that host large scheelite grains up to several cm in size; these grains preferentially crystallize at the contact between

quartz and surrounding rock (ESM Fig. 2b, c). Beryl also occurs locally in these veins (ESM Fig. 2c). The scheelites comprise both, disseminated mineralization (SD 650-19, SD 830-19 1-2, 570-40 85A) and mineralization in quartz veins (SD 625-19-1, SD 625-19 Be-2). Scheelite grains of this ore body predominantly belong to scheelite II, based on their luminescence colors. Scheelite III mostly occurs as rims on scheelite II (ESM Table 1). In lithoclast samples of the K2 ore body (K2) and in the SD-gneiss scheelite forms clusters along the foliation planes (ESM Fig. 1–3) and is mostly associated with quartz, albite, biotite, epidote-group minerals, and occasionally chlorite (ESM Fig. 5). Fluorite and calcite were also observed in the same layers as the scheelite, often associated and intergrown with scheelite grains. Apatite and titanite occur as accessory phases. Molybdenite is observed as a common accessory sulfide mineral in fractures and intergrown with scheelite (ESM Fig. 5a). It is best visualized in EPMA Mo-distribution maps (Fig. 3, 4e).

The K1-K3 hornblendite sample (Hbl) contains alternating actinolitized hornblende and quartz layers. Scheelite commonly occurs at the contact of both layers and is associated with muscovite (ESM Fig. 5d). Yellow fluorescent cores and blue rims belonging to scheelite II and III, respectively, are visible in shortwave UV light (Fig. 3e, f).

In the EOZ sample, scheelite is intensely stretched and forms recrystallized multigrain aggregates aligned along the finely laminated quartz layers. These layers form a planar texture (ESM Fig. 4a, b, 5c) and quartz grains show undulatory extinction and sub-grain rotation at grain boundaries (ESM Fig. 5c). Fluorescent color of these scheelite in this specimen is whitish-yellow. According to the existing scheelite classification, this scheelite belongs to generation I.

In all lithologies except the EOZ, scheelite displays brittle deformation features, such as undulatory extinction and fractures. These fractures are frequently filled with epidote-group minerals, quartz, chlorite, fluorite, and calcite. Scheelite recrystallization textures are rare (ESM Fig. 5c).

Qualitative and quantitative analyses of major and minor elements

Whole rock major and trace element analyses can be found in ESM Table A5 and C4. Scheelite Ca concentrations range from 19 to 20 wt% CaO with a median of 19.4 wt%. Tungsten concentration varies between 76 and 83 wt% WO_3 with a median of 79.6 wt% WO_3. Minor elements detected in this study are Sr and Mo. Scheelite EPMA analyses yield SrO between 0.02–0.21 wt% (ESM Table 2; ESM Table A). Molybdenum is the only minor element with significant concentrations and high variation throughout the measured grains ranging up to 3.0 wt%. These concentrations

correspond to a powellite ($CaMoO_4$) proportion of 1–4 mol% in scheelite (ESM Table 2, ESM Table A).

Scheelite microstructures in elemental and CL maps

Element distribution maps and quantitative analyses along zonation profiles in scheelite performed by EPMA combined with CL images demonstrate complex microstructures in scheelite grains and different types of zonation linked to Mo (Figs. 2, 3, 4). Cathodoluminescence is a valuable complementary method for scheelite characterization, because of the self-activated luminescence of scheelite (Gaft et al. 1998, 2005). The molybdate group in scheelite (MoO_4^{2-}; 470–560 nm) depresses the intensity of luminescence caused by the tungstate group (WO_4^{2-}; 450– 500 nm) which explains the overall lower intensity in Mo-rich scheelite and high CL intensities of Mo-poor scheelite (Poulin et al. 2016; Fig. 2h, k; Fig. 3, 4a-d). In color (hot CL) this results in either yellow or blue fluorescence (Fig. 4a, ESM Material CL). The color change from blue to yellow occurs between 0.4–0.8 wt% MoO_3 (Hsu and Galli 1973; Hsu 1977).

Scheelite generation I

Scheelite I sampled from the layered quartzite body contains whitish to pale blue fluorescent scheelite with $MoO_3<1$ wt% and lack any kind of zonation (Fig. 2a, ESM Material CL Figs. 3–4). A few grains contain pale yellow fluorescent scheelite in their centers (ESM Material CL Figs. 3, 4).

Scheelite generation II and III

Scheelite II was sampled in gneisses from the WOZ (orthogneiss "a"-SD-gneiss, orthogneiss "b"-felsic domains K2 lithoclast gneiss), amphibolite, and hornblende schist (Fig. 3, 4). The Mo-rich central area in EPMA maps corresponds to the yellow luminescent scheelite II (Fig. 4, ESM Material CL Figs. 1, 2, 5–8) and the Mo-poor scheelite overgrowth on the rims belong to scheelite III (Eichhorn et al. 1997). Most grains contain Mo-rich cores and a sharp contact to Mo-poor rims and Mo-poor fracture fills (~1.25–2 wt% and ~0–0.2 wt% MoO_3, respectively, Fig. 2d–l). Multigeneration scheelite grains (II core and III fracture fill and overgrowth; cf. Kozlik et al. 2016a) comprise a "simple" zonation. The maps visualize a regular zonation with an area of homogeneous, high Mo-scheelite (up to 3.0 wt% MoO_3) containing a powellite proportion of up to 4 mol% (ESM Table 2). Yellow scheelite cores are surrounded by irregular rims with lower Mo-concentration, both separated by sharp contacts (Fig. 2g-l, Fig. 3). Occasionally, scheelite II originating from orthogneiss "b" displays fine, oscillatory zoning
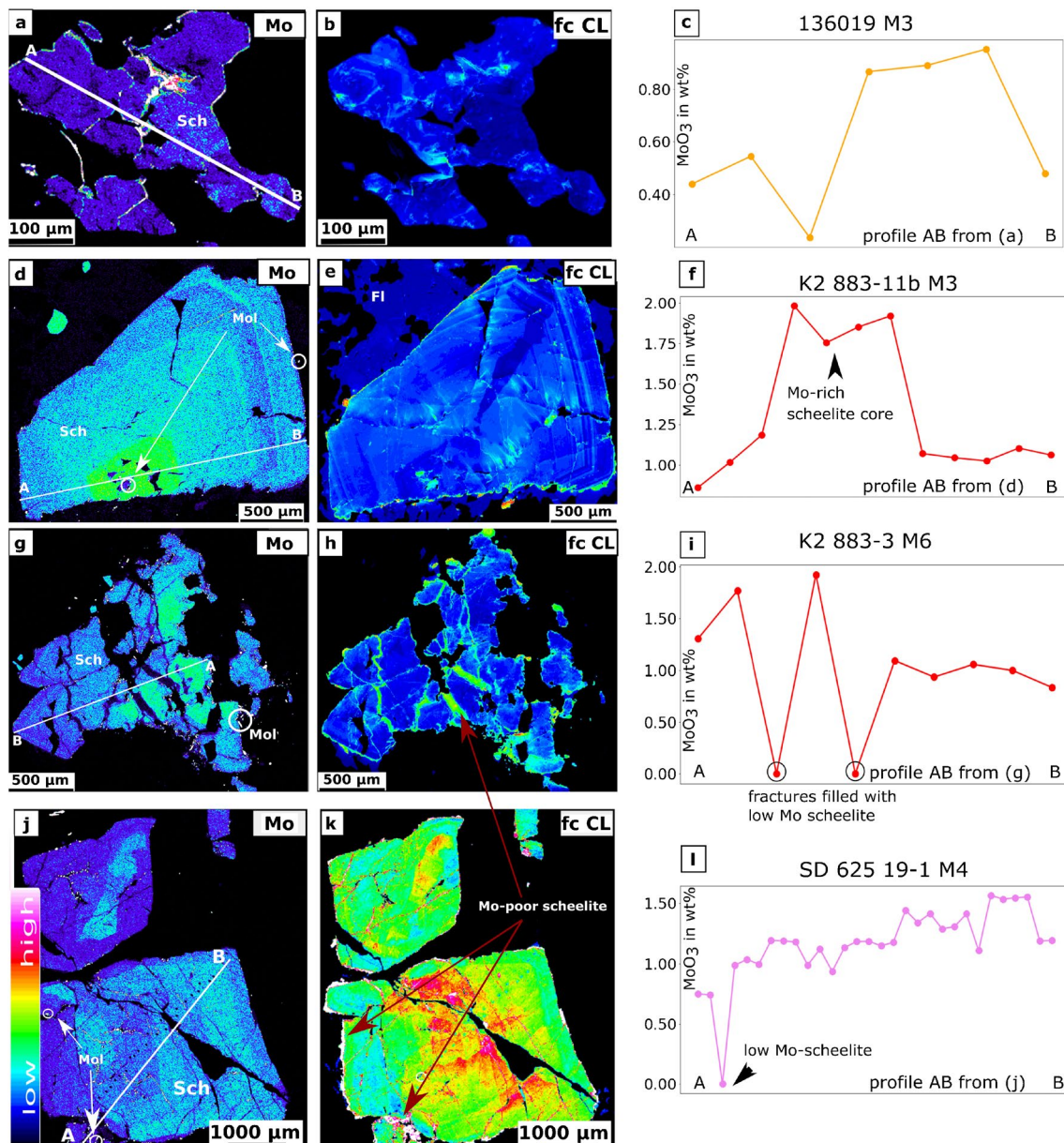
Fig. 2 Molybdenum distribution maps (WDS-EPMA), false color cathodoluminescence (fc CL) images, and quantitative MoO_3 concentrations (EPMA) of scheelite (Sch) along the indicated profiles. (**a-c**) Scheelite I grain (M3) with low Mo concentrations. (**d-f**) Scheelite II from orthogneiss "b" (M3 sample K2 883-11b) showing truncated oscillatory growth zonation and a Mo-rich core. Fluorite (Fl) surrounds the mineral grain. (**g-i**) Strongly truncated scheelite II from orthogneiss "b" (K2 883-3 M6) with refilled fractures (scheelite III) and molybdenite (Mol). (**j-l**) Complex scheelite in orthogneiss "a"-qtz vein -gneiss complex, partially truncated zonation, reflected by the MoO_3 profile. Note molybdenite (Mol) in fractures filled with scheelite III

in CL and the element distribution maps of Mo and is too fine to be resolved by EPMA (Fig. 2d–e).

Fractures filled with Mo-poor scheelite are often pervading the whole grain (Fig. 3, 4). Molybdenite crystals (0.5–5 µm across) are emplaced at the contact between the Mo-rich yellow and the Mo-poor blue fluorescent scheelite

(Figs. 2, 3, 4). Some scheelite grains show a rather irregular, patchy Mo-pattern in the cores (Fig. 2, Fig 4a, ESM Material CL Figs. 5–8) but also low Mo-rims (0.25 wt% in those rims, Fig. 4).
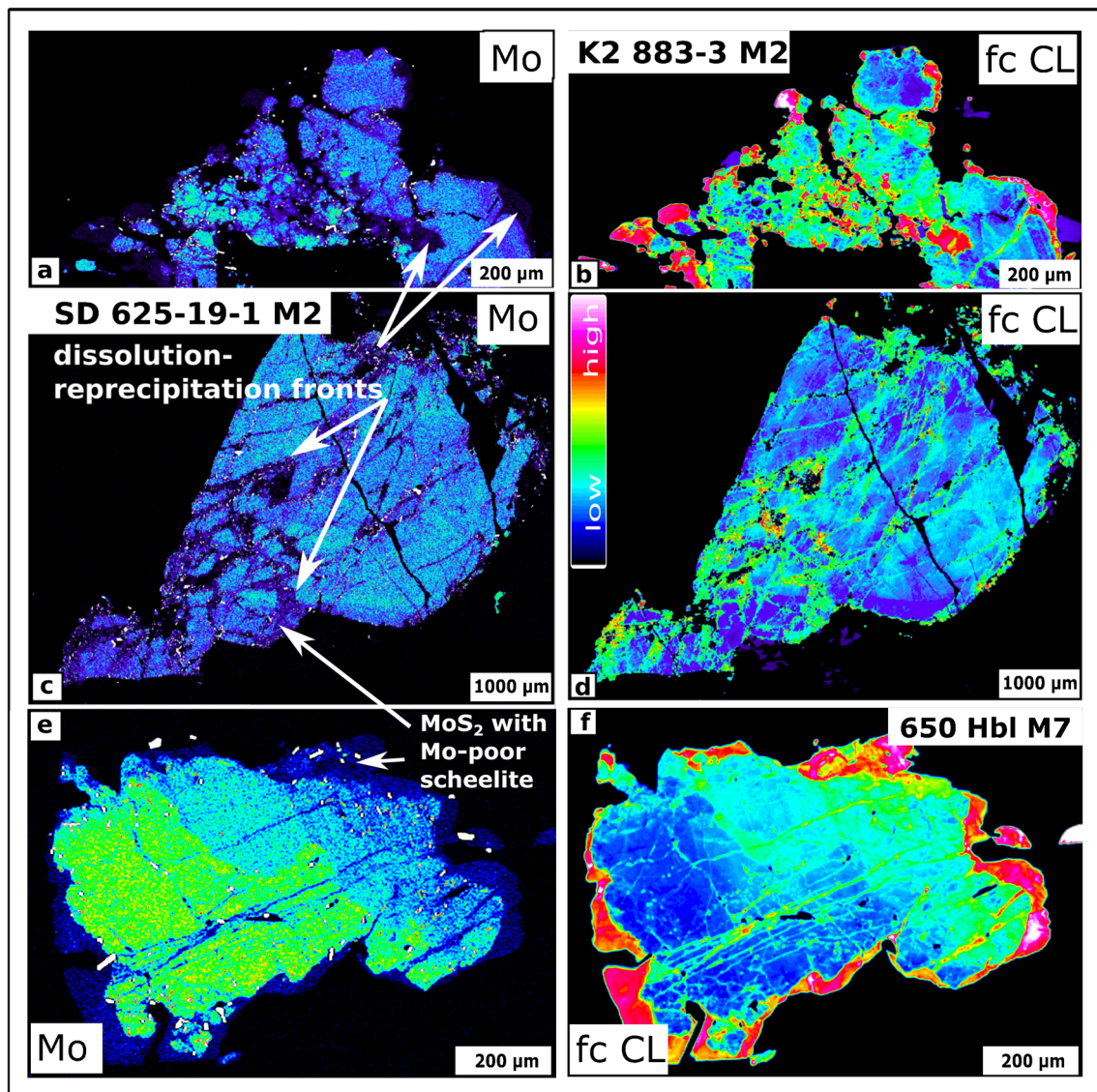
Fig. 3 Molybdenum distribution maps (WDS-EPMA) to the left and false color cathodoluminescence (fc CL) images to the right of scheelite affected by dissolution-reprecipitation fronts. Scheelite II and III from (**a-b**) orthogneiss "b" and (**c-d**) orthogneiss "a". Scheelite in hornblende schist (e-f, see ESM Fig. 5d). The lobate dissolution-reprecipitation front is in the center of the grain. Note molybdenite in Mo-poor zone

Scheelite generation IV

Chemical compositions of scheelite IV are very homogeneous and there was no zonation observed under UV light (ESM Figure 4c, d). WoO_3 concentrations are between 80–81 wt%, CaO between 19.5–19.8 wt%. Neither MoO_3, nor SO_3, SiO_2, and SrO were above detection limit (ESM Table 2).

Trace elements and Rare Earth Element (REE) distribution patterns in scheelite

The total-REE concentrations of Felbertal scheelite reach up to 2500 µg/g and the majority of the analyses range between 500 and 1000 µg/g (ESM Table 2; ESM Fig. 7c). A graphical representation of the normalized scheelite $(Gd/Ce)_N$ vs $(Gd/Lu)_N$ allows for the distinction of five significantly different REE patterns (Fig. 5; normalized to C1 from McDonough and Sun S -s. 1995). Those are (1) wing-shaped, (2) bowl-shaped, (3) flat pattern, (4) LREE-enriched, and (5) LREE depleted (Fig. 6). The numerical discrimination applied for
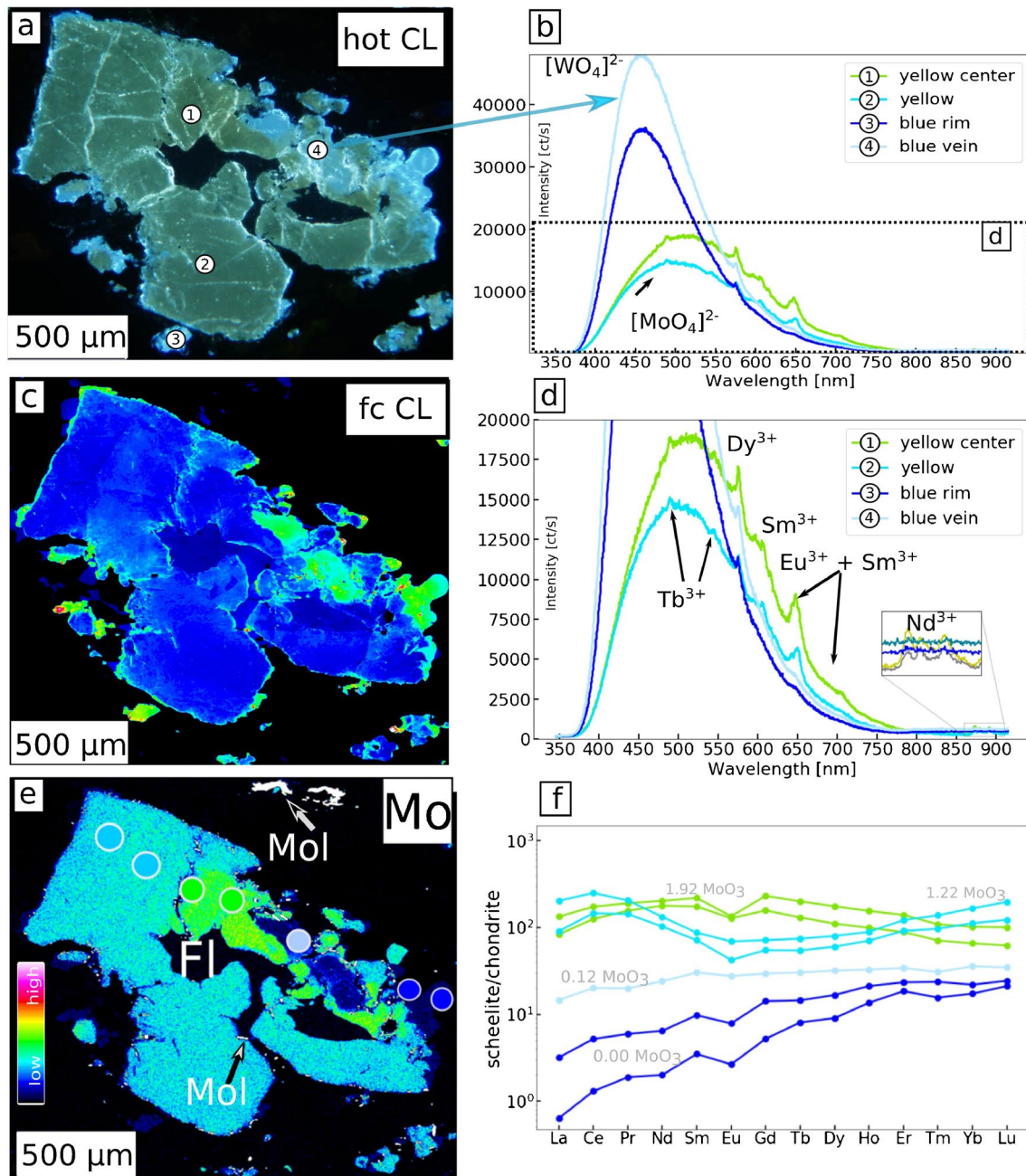
Fig. 4 Scheelite sample 883-11b M6 from K2 lithoclast gneiss analyzed with complementary imaging techniques. (**a**) Hot-cathode CL (hot CL) view with indications of measured areas 1–4 and the corresponding CL-spectra in (**b**, **d**). (**b**) CL spectra from locations 1–4 in (**a**) Yellow central parts of the grain (1, 2) correspond to broader, less intense peaks shifted towards higher wavelength by the molybdate functional group $[MoO_4]^{2-}$. Blue marginal parts (3, 4) with low Mo are dominated by the wolframate functional group $[WO_4]^{2-}$. (**c**) False color CL (fc CL) image view of EPMA WDS map. Fluorite (Fl) is present in the central fracture of the grain. Rim and fracture fill of the grain have high signal intensity. (d) Details of CL spectra in (**b**). Nar-row REE-peaks occur in the central parts (1, 2) of the grain (Tb^{3+}, Dy^{3+}, Sm^{3+}, Eu^{3+}, Nd^{3+}). Low Mo areas (3, 4) only contain Dy^{3+}. (**e**) Complementary EPMA Mo distribution map with irregular internal zonation and low Mo concentrations in the scheelite rim. Locations of LA-ICP-MS measurements and corresponding REE patterns are marked by colors. Molybdenite (Mol) grains are marked by arrows. Arrows in (**e**) indicated Mol in fractures occurring together with Mo-poor scheelite. (**f**) REE pattern of LA-ICP-MS analyses normalized to C1 chondrite (McDonough and Sun (1995). Colors correspond to locations in (**e**). Numbers are MoO_3 concentrations measured with EPMA
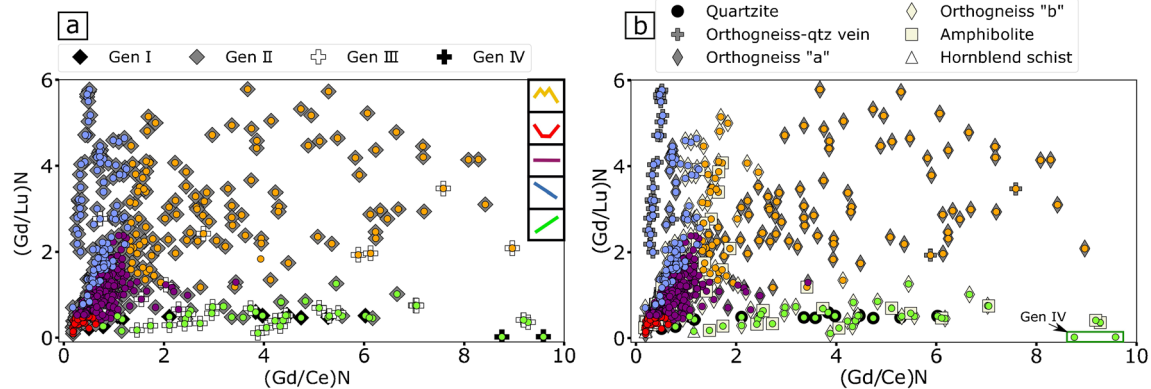
Fig. 5 Normalized Gd/Ce vs. Gd/Lu of scheelite analyses color coded by REE pattern type (wing-shaped: orange, bowl-shaped: red, flat: purple, LREE-enriched: blue, LREE depleted: green; colors in sketch grouping scheelite of each pattern is visualized in Figure 6 and details are explained in the ESM Material.

according to Fig. 6) sorted by (**a**) generation I–IV (Eichhorn et al. 1997) (**b**) by host-rock lithology (see text for details)

Scheelite trace element analyses were sorted according to generation I–IV (Schenk 1990; Eichhorn et al. 1997), REE pattern type, and host-rock lithology (Fig. 5, 6, 7, 8, ESM Table 2, ESM Fig. 6), which are quartzite (EOZ/ scheelite I), orthogneiss "a" (SD-gneiss), orthogneiss-qtz vein (>10 cm measuring qtz-veins in SD-gneiss), orthogneiss "b" (K2 lithoclast gneiss, felsic domains), amphibolite (K2 lithoclast gneiss, amphibolite domains), and hornblende schist. Generation I refers to scheelite from the EOZ (banded quartzite sample), generation IV is defined by scheelite samples IVa and IVb. Generation II includes scheelite grains with more than 0.2 wt% MoO_3. The concentration of MoO_3 in scheelite generation III is not clearly defined (cf. Eichhorn et al. 1997). Hence, generation III in our samples is any analysis with a MoO_3 concentration < 0.2 wt%, which had not been assigned to any other generation (cf. Schenk 1990; Eichhorn et al. 1997; ESM Table 3).

Scheelite generation I

Hot CL spectral data of scheelite grains from the layered quartzite show weak REE lines of Nd, Dy, and Sm (Fig. 4d) besides the main MoO_4 and WO_4 emission bands. The total REE of scheelite I yields up to 200 µg/g. From 22 LA-ICP-MS analyses of scheelite I most yield LREE-depleted patterns (n = 13; ESM Table 3). Bowl-shape and flat REE patterns occur subordinately (Fig. 5, 6).

Scheelite generation II-III

Scheelite with yellow color in hot-CL contains narrow REE lines in the spectra (Figs. 4b, d; ESM Table B). A clear qualitative distinction can be made between yellow fluorescent areas of scheelite II, which display lines of Nd^{3+}, Eu^{3+},

Dy^{3+}, Sm^{3+}, and Er^{3+}, and Tb^{3+}, and the blue fluorescent rims and fracture fillings of scheelite III (Gaft et al. 1998). The latter are poor in REE, with weaker REE^{3+} lines of Dy, Sm, and Nd (Fig. 4b; ESM Table B & ESM CL).

In the orthogneisses, scheelite mostly contains wing-shaped, bowl-shaped, and flat REE patterns (Fig. 5a; ESM Table 2). Scheelite II, which occurs in quartz layers as well as disseminated in orthogneisses, show LREE-enriched patterns (Fig. 5, 6). The scheelite III is mostly characterized by either LREE-depleted or flat patterns. Occasionally, scheelite III contains wing-shaped patterns (ESM Table 3).
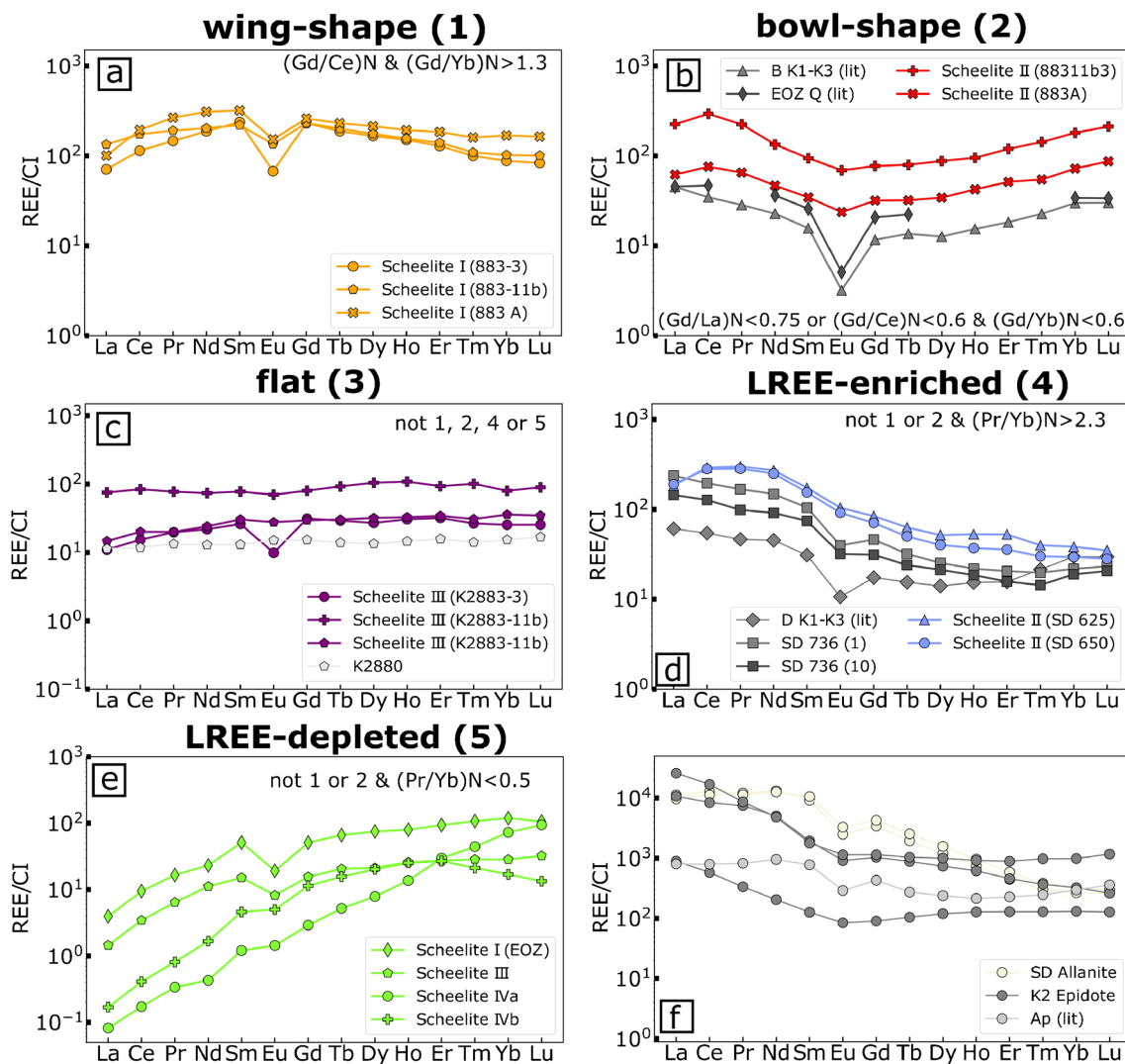
Scheelite generation IV

Scheelite IVa and IVb with whitish blue fluorescence color are exclusively characterized by LREE-depleted patterns (Fig. 6, ESM Table 3). LREE-depleted scheelite is characterized by low Mo-concentrations (<5000 µg/g), the highest CL-signals, and often pronounced negative Eu-anomalies (Fig. 6) and low total REE (ESM Table 3).

The vast majority of the analyzed scheelite samples of all generations in most lithologies have negative Eu anomalies between 0.1 and 0.9 (Fig. 7a; ESM Fig. 7). Occasionally, weak positive Eu-anomalies of up to 1.6 are observed in scheelite II and III in orthogneiss (K2) and amphibolite (Fig. 7a; ESM Fig. 7a) and are associated with flat and LREE-depleted patterns (Fig. 7a-b, ESM Fig. 7a-b, ESM Table 3). Positive Eu-anomalies correlate with high and low Mo concentrations (Fig. 7b), in scheelite II and III, respectively.

High field strength elements (Mo, Nb, Ta, Bi, Th, Y, and U)

The concentrations of Mo measured with EPMA and LA-ICP-MS correlate well within the analytical errors (ESM Fig. 8). Significant differences in some spots can be

Fig. 6 Chondrite-normalized REE types in Felbertal scheelite (**a–e**) with representative analyses and normalized characteristic element ratios for each pattern type and associated generation of scheelite (see discussion). REE patterns of host-rocks (**b–d**) and accessory minerals (**f**) for comparison. Note either absent or slightly negative Eu-anomalies. Color coding for each pattern type is transferred to Figures 5, 6, 7, 8 and ESM Figures: (**a**) wing-shaped pattern (1) in orange, (**b**) bowl-shaped pattern (2) in red plotted together with literature data (bright K1-K3 orthogneiss and EOZ quartzite), (**c**) flat pattern (3) in purple plotted with whole-rock data for orthogneiss "b" (K2880) (**d**) LREE-enriched pattern (4) in blue plotted with whole-rock analyses of orthogneiss "a" (SD 736) and literature data (whole-rock analysis from dark K1-K3 orthogneiss) (**e**) LREE-depleted pattern (5) (**f**) analyses of accessories: epidote-group minerals co-genetic with scheelite III, apatite from K1-K3 orthogneiss. Literature data (lit) taken from Kozlik (2015), Kozlik and Raith (2017), and von Quadt (1985)

attributed to different spot sizes and analytical volumes of the two techniques. The highest Mo concentrations have been detected in scheelite II from the orthogneisses and hornblende schist ($\geq$15000 µg/g; ESM Fig. 7b), whereas Mo is lowest in scheelite IV (IVa and IVb, median = 46 and 107 µg/g, respectively). Scheelite III contain low amounts of Mo (Fig. 3, 4, 5a; ESM Fig. 7b; ESM Table 3).

The Y concentration reaches up to 727 µg/g in scheelite II from orthogneiss "a", irrespective of the REE pattern type (ESM Fig. 7c). In contrast, relatively low Y concentrations are detected in scheelite from the orthogneiss "a"-quartz

vein, amphibolite and scheelite IV (~70 µg/g). The Y/Ho of orthogneisses "a" and "b" with wing-shaped and LREE-enriched pattern and samples of scheelite IVb are 13–23 (Fig. 8). Scheelite I, II from hornblende-schist with bowl-shaped patterns, and scheelite IVa display Y/Ho above the chondritic range (35–40).

Niobium and Ta are positively correlated in all samples (Fig. 7d, ESM Fig. 7d). Tantalum concentrations vary between 0.03 and 35.2 µg/g with a median of 1.96 µg/g (ESM Fig. 7d; ESM Table 2). Lowest Ta is observed in scheelite IV and in orthogneiss "a" of scheelite II (Fig. 7d,
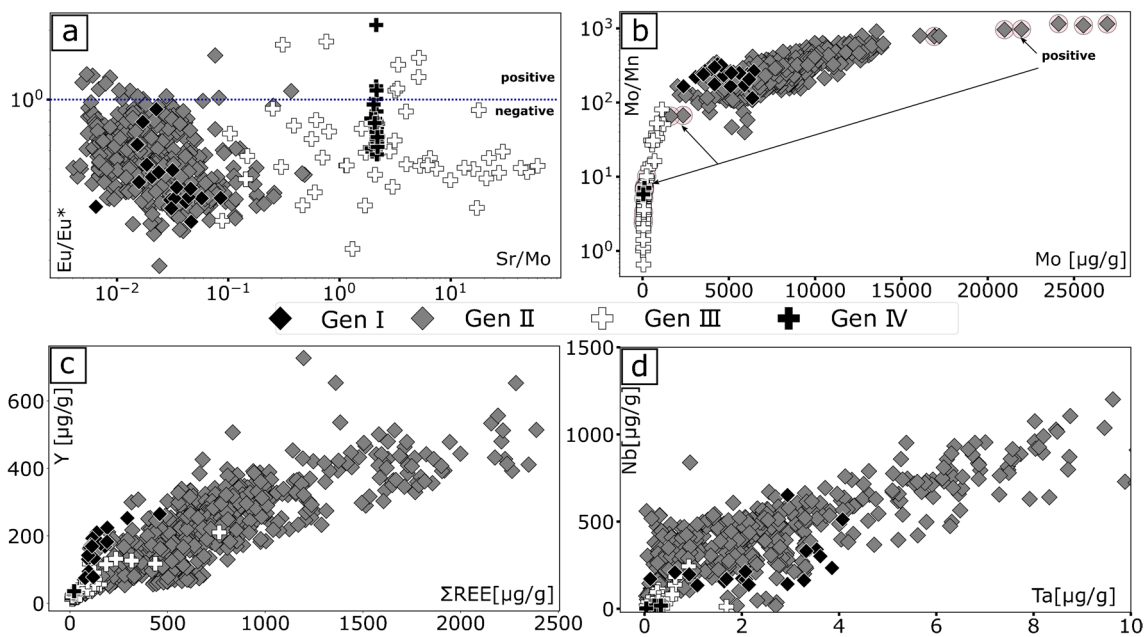
Fig. 7 Trace elements in scheelite sorted by generation I–IV (see legend in the center). (**a**) Sr/Mo vs. Eu-anomaly. Blue line marks shift from negative to positive Eu-anomaly. (**b**) Mo vs. Mo/Mn, circles mark analyses with positive Eu-anomalies. (**c**) total REE vs. Y (**d**) Ta vs Nb concentrations
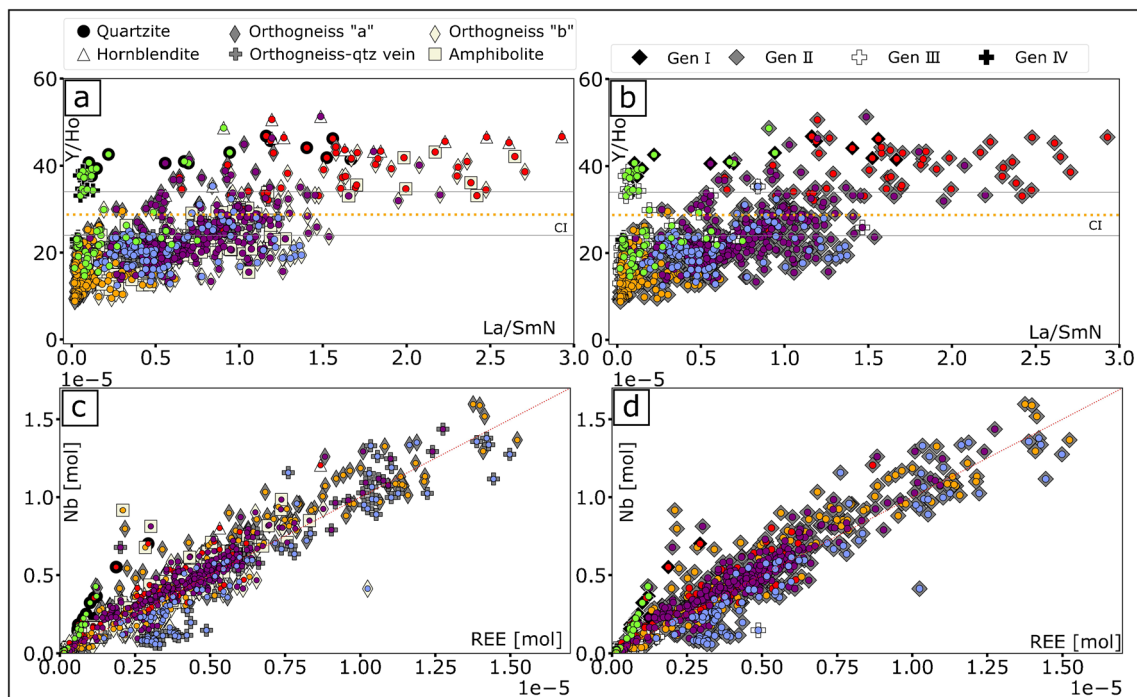
Fig. 8 Scheelite analyses assigned to REE pattern types: wing-shaped=orange, bowl-shaped=red, flat=purple, LREE-enriched=blue, LREE-depleted=green and scheelite analyses assigned to lithology or generation, as in Fig. 7. (**a-b**) (La/Sm)$_N$ vs. Y/Ho. Normalization to C1 chondrite (McDonough and Sun 1995). Chondritic range (CI) is marked after Bau (1996). Note supra-chondritic Y/Ho scheelite in the EOZ sample (scheelite I) (**c-d**) total REE[mol] vs. Nb[mol]. A medium molar weight of REE was chosen. Pearson correlation coefficient (R^2) between molar proportions of Mo and total REE for all data is 0.8

ESM Fig. 7d). Niobium concentrations show a wide spread between 1.8–1953 µg/g with a median of 376.5 µg/g. Scheelite I shows an almost constant Nb (200 µg/g Fig. 7a). Exceptionally high concentration up to 1200 µg/g are observed in scheelite II (Fig 7d). In general, there is a good correlation between molar Nb and total REE ($R^2 = 0.8$; Fig. 8c, d). The Nb/Ta covers a wide range of 4 orders of magnitude between 8 and 8946 with a median of 176. (ESM Table 2).

Uranium and Th concentrations are between 0.003 and 48.8 µg/g Th and up to 129 µg/g U, if these elements were detected above the lower limit of quantification (ESM Table 2, LOQ ~$3*10^{-3}$µg/g Th and $2*10^{-3}$ µg/g U). Median values are 1.16 and 1.01 µg/g, respectively. Uranium concentrations of above 10 µg/g were measured almost exclusively in scheelite from the EOZ. SD-gneiss scheelite samples with wing-shaped and flat REE patterns contain the second highest U concentrations (up to 15 µg/g). The lowest Th concentration is observed in scheelite with pattern type 5 of EOZ scheelite samples (~1 µg/g). Bismuth concentrations vary between 0.04–11.7 µg/g and Hf concentrations are 0.03–0.6 µg/g (ESM Table C).

Other trace elements

Strontium is highest in scheelite II from the orthogneiss "a" (up to 1678 µg/g ESM Fig. 6), while scheelite in the other lithologies ranges between 50 and 200 µg/g (ESM Table 2). Manganese is relatively low in scheelite I and IV (8–16 µg/g ESM Figure 6). Scheelite II contains up to 60 µg/g Mn, whilst generation III Mn concentration are between 20–40 µg/g. The highest Pb concentration is observed in scheelite I (quartzite) and occasionally in scheelite II with bowl-shaped and LREE-enriched patterns (90–140 µg/g ESM Figure 6). Scheelite with wing-shape, flat, and LREE-enriched REE patterns are characterized by low Pb concentration of 10–50 µg/g, belonging predominantly to scheelite III and IV.

Discussion

The new data enables us to combine microstructural observations with trace element data in scheelite from the Felbertal tungsten deposit and to get further insights into the petrogenetic evolution of its mineralization.

Precipitation and mobilization of scheelite

Scheelite microstructures

We argue that the intergrowth of scheelite II and III, as visualized by Mo-distribution maps and CL, results from a mineral-replacement process called fluid-mediated interface-coupled dissolution-recrystallization or reprecipitation (CDR, Putnis 2002). This interpretation agrees with the findings of Raith and Stein (2006), in contrast with models that propose an exsolution process (e.g., Höll 1975; Schenk and Höll 1991; Eichhorn et al. 1997). The paragenesis of Mo-poor and -free scheelite and molybdenite is evidence for the dissolution and in-situ replacement of Mo-containing scheelite by Mo-poor scheelite plus molybdenite in the presence of sulfur in the fluid phase. The process is illustrated by the intra-grain microstructures seen in CL and in WDS element maps in scheelite II and III in the WOZ (Fig. 2, 3, 4). By replacing the powellite-proportion of scheelite with almost pure, Mo-free scheelite, the morphology of the parent mineral is preserved and the chemical composition of the original mineral is only slightly altered. Our observation suggests that reprecipitation is incipient and localized (Fig. 2g, h; Fig. 3).

Volume changes, which are typically observed in minerals affected by CDR-processes (Putnis 2002), are not observed in scheelite. However, this is not exclusive for scheelite, but has also been described for other minerals, such as apatite and clinopyroxene (Harlov and Förster 2004; Harlov et al. 2005; Krause et al. 2013). CDR processes in metamorphic environments require porosity and permeability of the host rock to allow fluid transport, which can be created during the metamorphic event itself (Putnis and Austrheim 2010). The coupled dissolution-reprecipitation of scheelite is a polystage process that must have occurred related to secondary mobilization. We assume that it is linked to metamorphic fluids of Variscan age, since Re-Os ages of metamorphic molybdenite (associated with scheelite III) yield ages between ~ 342 and ~ 337 Ma (Raith and Stein 2006). This is further supported by a Sm-Nd errorchrone age of 319 ± 34 Ma for scheelite III (Eichhorn et al. 1997). Fluid inclusion studies suggest that Alpine fluids overprinted most scheelite, which could indicate that CDR processes and remobilization of W occurred multiple times (e.g., Schenk et al. 1990). The CDR process postdates oscillatory growth zoning, which was observed in scheelite from orthogneisses from the K2 ore body (Fig. 2d). We assume that the growth zoning originated from changing P-T-X conditions during initial mineral precipitation (Shore and Fowler 1996). Incomplete dissolution of scheelite and truncated zonation are characteristic for most analyzed scheelite grains (Fig. 2d, e; 3e, 4g), indicating localized recrystallization and hydrothermal alteration during metamorphism (Figs. 2, 3, 4). Since undulatory extinction affects the entire scheelite grains, we suggest that the last deformation event must have postdated the CDR process.

W mobilization

Trace elements in scheelite may help to distinguish primary from secondary re-mobilizing fluids. Direct analysis of the mineralizing fluid was not successful: Fluid-inclusion studies by Schenk et al. (1990) identified fluids of Alpine origin, based on composition and homogenization temperature. Fluid inclusions of primary scheelite have been overprinted during the poly-metamorphic history of the deposit. The gradual transition in the compatibility of REEs within scheelite observed in this study (pattern changing from 1-2-4 to 3 and 5; Fig. 6) reflects a transient change in ambient conditions and fluid chemistry (Hsu 1977; Ghaderi et al. 1999; Song et al. 2014). The first transition may have happened during the Variscan orogeny, as indicated by metamorphic molybdenite ages (~340 Ma, Raith and Stein 2006), which likely date the timing of the CDR process.

Scheelite solubility increases with rising temperature and NaCl concentration, while the effect of pressure is negligible (Gibert et al. 1992; Wood and Samson 2000). Due to the intense polyphase metamorphic overprint we have no direct access to the primary mineralizing fluid(s) in the Felbertal deposit. However, fluid-inclusion in other scheelite-only deposits reveal low salinities between 0–15 wt% NaCl eq. with Na likely dominating the electrolytes (Wood and Samson 2000). Additionally, the investigations have shown that mobilizing fluids are moderately acidic (i.e., low pH) with an oxidizing fO_2 between the quartz-fayalite-magnetite and the hematite-magnetite buffers (Gibert et al. 1992; Wood and Samson 2000).

These factors not only contribute to the first precipitation, but also have to be evaluated for the remobilization during the subsequent metamorphic overprint. Current models for the remobilization of scheelite in the Felbertal tungsten deposit postulate low pH and more reducing fO_2 for scheelite I compared to scheelite II, as well as scheelite III when compared to scheelite II (cf. Eichhorn et al. 1997). Scheelite can substitute Mo^{6+} for W^{6+}, which is promoted by relatively high fO_2, meaning that the stability of Mo-rich scheelite coincides with high fO_2 (Hsu and Galli 1973). Abundance of Mo^{6+} in scheelite is hence an indicator for high fO_2 during the precipitation of yellow fluorescent generations I and II (Eichhorn et al. 1997; Höll and Eichhorn 1998). A drop in pH (and fO_2) will have occurred between scheelite II and III: Scheelite II comprises Mo-enriched cores, where Mo^{6+} substitutes for W^{6+}, whereas the rims comprising scheelite III are Mo-depleted and coexist with molybdenite, in which Mo^{4+}, the reduced Mo oxidation state, is present (Figs. 2, 3, 4). Macroscopically, a shift from yellow to blue scheelite fluorescence can be seen, which accompanies this CDR processes (Eichhorn et al. 1997). In contrast, the change of environmental conditions between scheelite I and II (cf. Eichhorn et al. 1997) could not be verified by our observations.

The changing fO_2 is underlined by the slightly positive Eu-anomalies in high Mo and high Mo/Mn scheelite (Fig. 7b). Scheelite with both elevated Mo-concentrations and a positive Eu-anomaly, however, might not reflect the original geochemical signatures of the scheelite, since it is not known, if REE and Mo are similarly reactive during CDR processes. The variations reported in the Felbertal tungsten deposit are minor compared to global datasets (e.g., Sciuba et al. 2020; Miranda et al. 2022). Positive Eu-anomalies, which would indicate a reduced environment (Brugger et al. 2008; Su et al. 2020) do not exceed 1.6 in the analyzed scheelite samples and are rather erratic. Predominantly negative Eu-anomalies in scheelite from the Felbertal might record the preference of scheelite for Eu^{3+} over Eu^{2+} (Brugger et al. 2008) and the overall fingerprint of the host-rock lithology (Kozlik and Raith 2017). Interestingly, many of the scheelite samples of scheelite III and IV have positive Eu-anomalies (Fig. 7b). This could be explained by saussuritization of plagioclase during young Alpine metamorphism (Shatagin and Volkov 2020), which causes an increase of Eu^{2+} in the fluid and positive Eu-anomalies in scheelite of that age. However, the change in the Mo/Mn between scheelite I and II, and III and IV indicates a significant change of the geochemical conditions, and be a response to the shift from a magmatic hydrothermal to metamorphic hydrothermal environment, accompanied by a change in fO_2 (ESM Fig 7a, b). A shift from oxidizing to reducing and more acidic conditions, possibly due to a change from primary magmatic to metamorphic stage (cf. Poulin et al. 2018) would coincide with an increase of free H^+ (low pH), which would in turn destabilize scheelite. Tungsten will be transported as long as complexes can be held in solution, meaning the reprecipitation of scheelite again depends crucially on factors like availability of ligands in the fluid, pH, fO_2, temperature, and pressure.

Effect of fluorine

Kozlik and Raith (2017) proposed that the first magmatic fluids must have contained significant amounts of F, based on elevated F-concentrations in W-mineralized K1-K3 orthogneiss (≤4438 µg/g). Fluorine is known to increase the solubility of the HFSE, such as Ti, Nb, and Ta in fractionated granitic melts (Breiter et al. 1999; Ballouard et al. 2016). It further increases the solubility of HFS element sinks, such as titanium oxides and zircon (Keppler 1993; Rapp et al. 2010), which are also present in the Felbertal tungsten deposit (Kozlik 2015; Kozlik et al. 2016b). It will also lower the crystallization temperature of accessory phases, which will enhance the redistribution of incompatible elements in a hydrothermal-magmatic environment (Agangi et al. 2010). Hence, F played an important role during mineralization, fostering incompatible behavior and the concentration of

lithophile elements in the residual magmatic liquid upon fractionation. Complexing agents like Cl, H_2O, and alkalis must have transported the immobile elements (W, Nb, Ta, REE) into the fluid phase during the late magmatic stage (Irber 1999; Wood and Samson 2000; Agangi et al. 2010).

The Y/Ho in scheelite from the Felbertal varies between 9–50 (Fig. 8a, b), which might indicate fluid-rock interaction (Xiao et al. 2022), as well as fluid speciation, which controls the complexation of REE and HFSE in a fluid (Bau 1996). High Y/Ho (≤200) in hydrothermal vein fluorite has been attributed to the elevated stability of Y-F complexes compared to Ho-F in aqueous systems (Walker and Choppin 1967). Hence, elevated Y/Ho in scheelite could be an indicator for the presence of F in the fluid (Bau 1996). High Y/Ho characterize scheelite I and scheelite characterized by bowl-shaped REE pattern from scheelite II (Fig. 8). Scheelite I also show intense recrystallization, which together with high Y/Ho might indicate intense hydrothermal alteration of the quartzite host-rock and scheelite minerals in the EOZ (Fig. 9). Low to moderate Y/Ho (10–35) of scheelite from orthogneisses in the WOZ might indicate fluid-wallrock interaction (see below), since whole-rock data are similar (25–31 ESM Table C; 31–38 Kozlik and Raith 2017).

We know most certainly that F was present in late hydrothermal metamorphic fluids, since fluorite is observed in association with scheelite (ESM Fig. 5, Höll and Schenk 1988). We observed fluorite associated with scheelite III (Fig. 4). This corroborates the fact, that F-rich aqueous complexes are most prominent at lower temperatures (Loges et al. 2013), indicating their relevance for later stages of scheelite remobilization and alteration (Fig. 3, 4), as suggested by Schenk et al. (1990). However, additional data are needed to elucidate this hypothesis.

Niobium and Ta, as discussed above, could have been enriched in late magmatic fluids, together with W, due to the presence of F. Nb/Ta in scheelite of the Felbertal deposit spread across four magnitudes (1–2500 ESM Table 1) and are in strong contrast with published values for scheelite from other deposits (0.01–0.04 Su et al. 2020 and ~ 64 Sciuba et al. 2020). It is important to point out that Ta concentrations are affected by an abundance sensitivity of ^{180}W and ^{182}W on ^{181}Ta, which leads to systematically overestimated Ta concentrations and in turn underestimated Nb/Ta (ESM Material). In particular, low Ta contents are affected by the above-mentioned effect. To our knowledge, this has not been corrected for in other studies. Hence, we assume that the comparability of our data with other studies might be impeded. In our study, high Nb/Ta is characteristic for scheelite II with highest absolute Nb and total REE and wing-shaped and LREE-enriched pattern (Fig. 8), which might belong to primary scheelite, when considering one primary mineralizing event and all successive events only remobilize the scheelite. The enrichment of Nb might reflect the acting substitution mechanism (see below). Textural evidence indicates, that some biotite pre-dates scheelite crystallization. LA-ICP-MS data of this study from micas
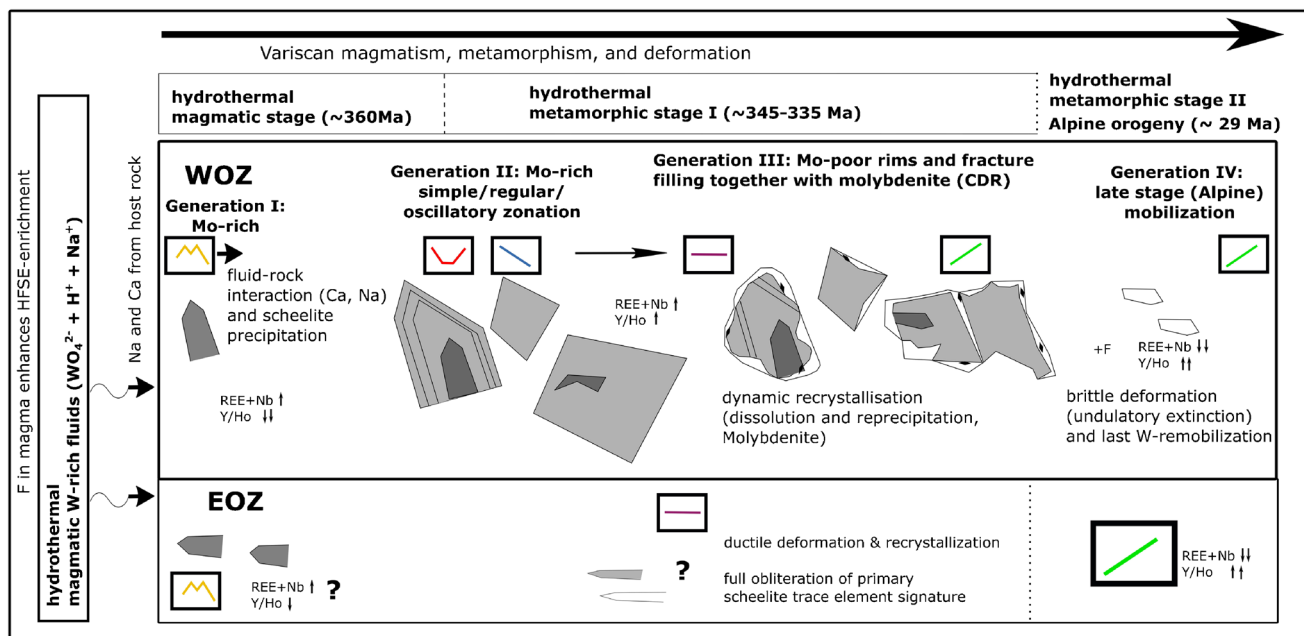
Fig. 9 Schematic illustration of the genetic relation between scheelite I–IV in both ore zones of the Felbertal W deposit (WOZ and EOZ). REE pattern: wing-shaped (yellow), bowl-shaped (red), LREE-enriched (blue), flat (violet), and LREE-depleted (green). See text for detailed description

near scheelite of the orthogneisses have Nb/Ta>1000 (ESM Table C). Tungsten concentrations in micas are very low (<4 µg/g in biotite of the orthogneisses; ESM Table C). Niobium enrichment in scheelite could originate not only from the fluid, but also from alteration of primary, magmatic micas.
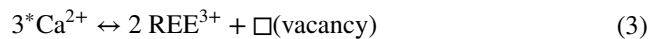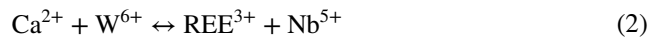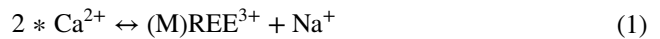
Nb/Ta are high in our whole-rock analyses (orthogneisses: SD-gneiss ~28, K2 Brekzie ~ 50; ESM C). This enrichment could indicate an accumulation of biotite in these lithologies during metamorphism (Ballouard et al. 2020). Biotite and muscovite preferentially incorporate Nb over Ta and thereby fractionate Nb from Ta (Stepanov et al. 2014; Ballouard et al. 2020). Metamorphic biotite is very common in most ore bodies in the deposit as a remnant of metamorphic recrystallization. In contrast, literature values of the K1-K3 orthogneiss, which is thought to be closely related to the mineralizing magmatic fluid, reveal low Nb/Ta (5–10; Kozlik and Raith 2017). These values underline the highly fractionated character of the K1-K3 orthogneiss and its potential to be the source of the first scheelite mineralization linked to magmatic-hydrothermal fluids (Kozlik 2015; Kozlik and Raith 2017).

Rare earth elements (REE) in scheelite

Different abundances of REE species in the CL spectra accompany the change in fluorescence color from yellow cores to and blue rims. The Mo-rich, yellow fluorescent scheelite cores contain peaks belonging to Sm, Eu, Dy, Tb, and Nd, whereas the blue fluorescent rims only show a peak belonging to Dy (Fig. 4d). The CDR process most likely causes a redistribution of REE from pristine scheelite towards reprecipitated, secondary scheelite. As already indicated by the qualitative differences of REE in hot-CL spectra, it is possible to differentiate between five different REE patterns in scheelite from the Felbertal mine, which do not necessarily correspond to the previously defined scheelite generations (ESM Table 1). As such, the existing scheelite classification of four generations is to be discussed in the light of trace element incorporation into scheelite.

Individual scheelite grains of generation II have wing-shaped and bowl-shaped REE patterns, which change towards flat and LREE-depleted REE patterns (Fig. 4f). The REE patterns themselves give additional information about the geochemical environment during scheelite (re-)precipitation. All microstructural and geochemical observations indicate a complex and polyphase mineralizing system. The crystal structure of scheelite consists of tetrahedral groups of $[WO_4]^{2-}$ and irregular dodecahedral groups of $[CaO_8]^{14-}$ (Ghaderi et al. 1999 and references therein). Calcium can be replaced by isovalent substitution of Sr, Mn, As, or Ba and heterovalent substitution with REE and Y (Nassau 1963; Kempe et al. 1991; Uspensky et al. 1998; Ghaderi et al. 1999). The distinction of different REE patterns in scheelite

(Fig. 4, 6) indicates an apparent genetic complexity (e.g., Brugger et al. 2000; Su et al. 2020). Three different substitutions have to be considered (Ghaderi et al. 1999):

$$2 * Ca^{2+} \leftrightarrow (M)REE^{3+} + Na^+ \qquad (1)$$

$$Ca^{2+} + W^{6+} \leftrightarrow REE^{3+} + Nb^{5+} \qquad (2)$$

$$3 * Ca^{2+} \leftrightarrow 2\,REE^{3+} + \square(vacancy) \qquad (3)$$

Scheelite is prone to fractionate MREE because the scheelite-liquid partition coefficients for MREE are higher than those of light and heavy REE (Nassau and Loiacono 1963). As a consequence, MREE-enriched patterns (equivalent to REE pattern type 1/ wing-shape), are indicative for the oldest scheelite generations. This corroborates with a study of Raith et al. (2011) who found that a wing-shaped REE pattern is characteristic for scheelite I (Eichhorn et al. 1997). As soon as the REE budget of the fluid changes the patterns are likely to change, too (Fig. 9). Other studies are in agreement with this assumption, discussing that wing-shaped patterns (1; Fig. 4, 6) in scheelite are indeed most common for primary scheelite (Ghaderi et al. 1999; Brugger et al. 2000). In experiments, the preferred fractionation of MREE includes the presence of alkali-elements (Nassau 1963; substitution mechanism 1). If a wing-shaped REE pattern is typical for scheelite I following substitution type (1), Na should correlate with the total REE concentration of scheelite (Ghaderi et al. 1999). The Na-involving substitution mechanism, responsible for a MREE-pronounced pattern, does not require vast amounts of Na. Concentrations in scheelite with similar wing-shaped pattern have been reported to be in the range of 130-280 µg/g (Ghaderi et al. 1999). The concentration of Na in scheelite from the Felbertal is below the lower limit of quantification (~ 250 µg/g) and mostly below the detection limit of 75 µg/g of the EPMA and hence it is impossible to quantitatively characterize the Na-REE substitution mechanism. Nevertheless, it remains relevant when considering that tungsten is mobilized as an oxy-anion complexing with K^+, Na^+ or H^+ (Gibert et al. 1992; Hulsbosch et al. 2016; Lecumberri-Sanchez et al. 2017). These ions are considered essential for the transport of HFSE and W, but not for the incorporation of REE into scheelite. To our knowledge, experimental data regarding the influence of Na on the fractionation of REE in scheelite are not available yet.

The progressive depletion in MREE observed from the core towards the rim translates to a transition from a wing-shaped REE-pattern to bowl-shaped or LREE-enriched patterns, indicating a change in the substitution mechanism (Fig. 4f). Hence, Na might have played an important role for first scheelite precipitation (Lecumberri-Sanchez et al. 2017), but it seems to be of minor importance for

remobilized scheelite during CDR. A wing-shaped REE pattern is mostly preserved within cores of bright yellow luminescence in scheelite II from orthogneisses (SD-gneiss and K2) (Fig. 4, 6; ESM Table 3). Scheelite II contains not only wing-shaped patterns, but also flat, LREE-enriched, bowl-shaped, and rarely LREE-depleted patterns (Fig. 4, 6b; ESM Table 3). We do not observe any quantitative increase of REE from cores to rims (Fig 4f). This may indicate that after the first influx of hydrothermal fluids reflected by wing-shaped patterns, scheelite was only re-mobilized and no new influx of W-enriched fluids occurred (cf. Xiao et al. 2022). Interestingly, the typical scheelite I sample we studied (EOZ Sample ID: 136019) predominantly contains scheelite with LREE-depleted patterns. There might be two reasons: (1) Although our sample corresponds to the typical EOZ "Reicherz" on a macroscopic scale, its trace element characteristics might have been altered during polymetamorphic overprint of the deposit, which is underlined by quartz-recrystallization textures (ESM Fig. 5c); (2) The EOZ bears a variety of trace element characteristics, which has not been sampled thus far. A careful study of scheelite from the EOZ is beyond the scope of this study, but our findings indicate that any conclusions about scheelite from the EOZ need to be drawn with caution. The absence of wing-shaped patterns of scheelite I does not necessarily prove that primary scheelite is absent in the EOZ. Besides substitution mechanism (1), which is linked to the precipitation of the wing-shaped REE pattern, we observe a good correlation of $\sum$ REE and Nb in scheelite (Fig. 8c, d). This indicates that substitution (2) is the dominant substitution mechanism for REE into scheelite at the Felbertal (Ghaderi et al. 1999). The correlation is only slightly offset in scheelite II with LREE-enriched pattern from orthogneiss-qtz vein and is steeper for LREE-depleted pattern in scheelite I. This could indicate that other substitution mechanisms were predominant (Fig. 8c). A flat REE pattern, which is observed in generation II and III, could indicate an episode without REE fractionation or just a transition from a wing-shaped pattern to a LREE-depleted pattern (Fig. 4f).

Host-rock interaction and scheelite paragenesis

At the Felbertal, first scheelite deposition is likely related to felsic intrusions in the course of the Variscan orogeny (Kozlik and Raith 2017). Experimental and theoretical studies show that in granite-related magmatic-hydrothermal systems W is transported as hydrated oxy-anion complexes (H_2WO_4 ~ HWO_4^- and WO_4^{2-}), as the volatiles degas from highly fractionated melts (Bernard et al. 1990; Gibert et al. 1992; Wood and Samson 2000; Kazamel et al. 2023). In these environments, W solubility can reach values up to thousands of µg/g if W is transported in a hydrated species which complexes with Na^+ (Wood and Samson 2000). Subsequent

scheelite deposition may occur after the chemical equilibration of the fluid with a Ca-rich host-rock due to an increase in Ca-activity upon fluid-rock interaction (Gibert et al. 1992; Lecumberri-Sanchez et al. 2017). This indicates that host-rocks recording enhanced fluid-rock interaction may be co-genetic to scheelite I and II. Accordingly, we assume that scheelite formation at the Felbertal was enhanced by the presence of abundant Na and Ca in the host-rock and the availability of Na as transporting ligand in the mineralizing hydrothermal system (Na_2O: 2.55–5.94 wt% in the mineralized K1-K3 orthogneiss: Kozlik and Raith 2017, 2.36 wt% in K2 lithoclast gneiss, 4.74–5.45 wt% in the SD-gneiss; CaO: 5–7 wt% in the surrounding orthogneisses; ESM Table A, Fig. 9). The availability of REE during scheelite precipitation is a major factor controlling the shape of REE-patterns in scheelite (Fig. 9) and usually reflects the bulk trace element concentrations in the host-rock (Raimbault et al. 1993; Lecumberri-Sanchez et al. 2017; Leng et al. 2018; Sciuba et al. 2020). Consequently, different lithologies (e.g., igneous or sedimentary) may result in a specific trace element signature in scheelite (cf. Poulin et al. 2018). Preliminary results from a limited number of whole rock samples, as well as a compilation of literature data (Fig. 6) reveal that bowl-shaped REE pattern in scheelite II are characteristic for e.g., bright K1-K3 orthogneiss (Fig. 6b), whereas LREE-enriched pattern in scheelite II and III are similar to the dark K1-K3, quartzite, and orthogneiss "a" (SD-gneiss) REE patterns (Fig. 6d). The orthogneiss "b" (K2880) yields a rather flat REE patterns (Fig. 6c). In contrast, wing-shaped REE patterns (1) are not detected in any host-rock lithology, pointing to a genetic relationship with a primary, external fluid source (Fig. 9). Contrarily, secondary scheelite generations more likely reflect the REE budget of the host-rock lithologies due to intense fluid-rock interaction (Fig. 6). Comparison with accessory phases like apatite, titanite, and epidote-group minerals that are co-genetic with scheelite III and IV reveals that the trace element budget is not only governed by fluid-rock interaction, but also by competing mineral phases, that act as REE sinks (Fig. 6f). Apatite, titanite, and epidote-group minerals (ESM Material CL Fig. 2) are very compatible with LREE. The apatite REE pattern originating from K1-K3 orthogneiss is similar to LREE-enriched scheelite patterns and the whole rock REE trace element pattern of dark K1-K3 orthogneiss (Fig. 6f). Epidote associated with chlorite occurs in fractures that cross-cut yellow-fluorescent scheelite and its blue fluorescent scheelite rims (generation II and III). As a typical assemblage for lower amphibolite to greenschist metamorphic facies, it is related to the latest retrograde metamorphic overprint. Analyzed epidote REE patterns are LREE-enriched, which agrees with the LREE-depleted patterns of latest scheelite III and IV (Fig. 6f, ESM C). This indicates that both minerals co-precipitated during the last phase of scheelite mineralization, supporting a

metamorphic formation of scheelite III and IV under green-schist to amphibolite facies conditions (Fig. 9). This is also in agreement with the observation of epidote inclusions in the late stage scheelite IV. Greenschist facies metamorphic conditions prevailed during the Variscan metamorphism (Eichhorn et al. 1995; Raith and Stein 2006). During the Alpine orogeny, the rocks of the Habach Complex in the Tauern Window were metamorphosed under amphibolite (peak metamorphism) and greenschist (retrograde) facies conditions (von Raumer et al. 2013), meaning that the REE pattern and phase assemblage could be an evidence of either Variscan or Alpine metamorphism (Fig. 9). Since we consider that Alpine metamorphism overprinted Variscan metamorphic remnants, we argue that an LREE-depletion in scheelite might be the result of the latest metamorphic fluids, which scavenged LREE and Mo from scheelite (Fig. 9). A strong argument for this hypothesis is the observation that scheelite III and IV is characterized by LREE-depleted pattern (ESM Table 3) (Eichhorn et al. 1997; Raith and Stein 2006). Hence, we further suspect that not only scheelite II and III, but also scheelite I eventually suffered from hydrothermal alteration during the Variscan orogeny and was subsequently altered by Alpine metamorphism (Fig. 9). The last metamorphic episode will also have caused scheelite deformation in the WOZ (undulatory extinction), which affects scheelite II and III in the same way. Subsequent scheelite with a trace element signature of scheelite IV might exist not only as isolated grains, but also as obliterated Mo-free scheelite III rims, or even have obliterated scheelite, which texturally unequivocally belongs to scheelite I (compare scheelite REE pattern of the quartzite sample, Fig. 9).

Scheelite – a global tracer mineral for ore deposit discrimination and exploration targeting?

Various geochemical ore-deposit discriminators have been proposed for scheelite (e.g., Poulin et al. 2018; Sciuba et al. 2020; Miranda et al. 2022). Sr/Mo ratios of scheelite from the Felbertal deposit ranges between 0.004–60.4, with most scheelite plotting between 0.02 and 11 (Fig. 7a, ESM Fig. 9). This combined with predominantly negative Eu-anomalies would classify the Felbertal scheelite exclusively as magmatic-hydrothermal (ESM Table 2, 3; Poulin et al. 2018 Fig. 16D). Similarly, applying the Mo and Sr discrimination plot by Miranda et al. (2022) also points to an exclusively magmatic-hydrothermal origin of the Felbertal scheelite. Compared to a global dataset (Sr: 5-10^{4}μg/g, Miranda et al. 2022), the range of Sr and Mo in the Felbertal is minor (0–500 μg/g Sr, Fig. 6 and 0–25000 μg/g Mo, Fig. 7b, ESM Fig. 9). Since we know that the Felbertal scheelite was overprinted by multiple metamorphic fluids, we consider the classifications not applicable to the Felbertal mine.

Consequently, polymetamorphic deposits, like the Felbertal tungsten deposit, cannot be classified using the introduced discriminators, as their trace element budget has likely been distorted during multiple metamorphic events. This highlights the need for a careful evaluation of scheelite trace element data before deducing genetic conclusions.

Conclusions

(1). Four generations of scheelite (scheelite I–IV) from the Felbertal tungsten mine, sampled from several ore bodies, display complex genetic relations based on quantitative element and CL maps. Molybdenum is highly variable throughout the different generations of scheelite and the only element responsible for changes in CL intensity and fluorescence.

(2). Five different REE pattern types in scheelite are evidence for the redistribution of REE as a consequence of changing P-T-X compositions of metamorphic fluids and host-rock interaction after the initial magmatic-hydrothermal mineralization. A wing-shaped REE pattern, which is attributed to the initial scheelite mineralization, was observed only in scheelite II from the western ore field (Fig. 9). Scheelite II also contains bowl-shaped and LREE-enriched patterns, which coincide with host-rock REE indicating host-rock interaction of the mineralizing fluid during magmatic and successive metamorphic stages. Scheelite III formed during W-remobilization during metamorphism and is the product of a dissolution-reprecipitation process of older scheelite generations I and II. Along this process, REE were redistributed and scheelite is characterized by mainly flat and LREE-depleted pattern (Fig. 6, 9). An LREE-depleted pattern is also characteristic for scheelite IV.

(3). LREE-depleted pattern in scheelite I from the EOZ are attributed to a more pronounced metamorphic overprint of quartzite host-rocks, compared to amphibolite and orthogneiss host-rocks. This is underlined by scheelite recrystallization and deformation textures (Fig. 9).

(4). Eu-anomalies in scheelite vary between 0.2–2.1 and mostly reflect the negative Eu-anomaly of the host-rock. Elevated Y/Ho (38–58) were observed in scheelite I and scheelite II showing bowl-shaped REE patterns, indicating progressive hydrothermal alteration. Most scheelite of generations II, III, and IV have Y/Ho between 10–30. Values below the host-rock range (24–33) might indicate vast fractionation, just as the Nb/Ta ratios, which span over four magnitudes. The dominant substitution mechanism for REE into scheelite from the Felbertal is the coupled substitution of $REE^{3+} + Nb^{5+}$ for $Ca^{2+} + W^{6+}$.

(5). Geochemical indicator elements proposed in litera-
ture, like Mo and Sr, are not applicable for the dis-
crimination of the origin of mineralizing fluids from
the Felbertal tungsten deposit.

Declarations

References

Agangi A, Kamenetsky VS, McPhie J (2010) The role of fluorine in
the concentration and transport of lithophile trace elements in
felsic magmas: Insights from the Gawler Range Volcanics, South
Australia. Chem Geol 273:314–325. https://doi.org/10.1016/j.
chemgeo.2010.03.008

Ballouard C, Massuyeau M, Elburg MA et al (2020) The magmatic
and magmatic-hydrothermal evolution of felsic igneous rocks
as seen through Nb-Ta geochemical fractionation, with implica-
tions for the origins of rare-metal mineralizations. Earth-Sci Rev
203:103115. https://doi.org/10.1016/j.earscirev.2020.103115

Ballouard C, Poujol M, Boulvais P et al (2016) Nb-Ta fractionation
in peraluminous granites: A marker of the magmatic-hydrother-
mal transition. Geology 44:231–234. https://doi.org/10.1130/
G37475.1

Bau M (1996) Controls on the fractionation of isovalent trace elements
in magmatic and aqueous systems: evidence from Y/Ho, Zr/Hf,
and lanthanide tetrad effect. Contrib Mineral Petrol 123:323–333

Bernard A, Symonds RB, Rose WI (1990) Volatile transport and depo-
sition of Mo, W and Re in high temperature magmatic fluids.
Appl Geochem 5:317–326. https://doi.org/10.1016/0883-2927(90)
90007-R

Breiter K, Förster H-J, Seltmann R (1999) Variscan silicic magma-
tism and related tin-tungsten mineralization in the Erzgebirge-
Slavkovskỳ les metallogenic province. Mineral Deposita
34:505–521

Brugger J, Etschmann B, Pownceby M et al (2008) Oxidation state
of europium in scheelite: tracking fluid–rock interaction in gold
deposits. Chem Geol 257:26–33

Brugger J, Lahaye Y, Costa S et al (2000) Inhomogeneous distribu-
tion of REE in scheelite and dynamics of Archaean hydrothermal
systems (Mt. Charlotte and Drysdale gold deposits, Western Aus-
tralia). Contrib Mineral Petrol 139:251–264

Eichhorn R, Höll R, Jagout E, Schärer U (1997) Dating scheelite stages:
A strontium, neodymium, lead approach from the Felhertal tung-
sten deposit, Central Alps, Austria. Geochim Cosmochim Acta
61:5005–5022. https://doi.org/10.1016/S0016-7037(97)00349-9

Eichhorn R, Höll R, Loth G, Kennedy A (1999) Implications of U-Pb
SHRIMP zircon data on the age and evolution of the Felber-
tal tungsten deposit (Tauern Window, Austria). Int J Earth Sci
88:496–512. https://doi.org/10.1007/s005310050281

Eichhorn R, Schaltegger U, Höll R (1995) Age and evolution of
scheelite-hosting rocks in the Felbertal deposit (Eastern Alps):
U-Pb geochronology of zircon and titanite. Contrib Mineral Petrol
119:377–386. https://doi.org/10.1007/BF00286936

Fedorowich JS, Richards JP, Jain JC et al (1993) A rapid method for
REE and trace-element analysis using laser sampling ICP-MS
on direct fusion whole-rock glasses. Chem Geol 106:229–249.
https://doi.org/10.1016/0009-2541(93)90029-I

Finger F, Steyrer HP (1988) Granite-types in the Hohe Tauern (Eastern
Alps, Austria) — Some aspects on their correlation to Variscan
plate tectonic processes. Geodin Acta 2:75–87. https://doi.org/10.
1080/09853111.1988.11105158

Finger F, Waitzinger M, Förster HJ et al (2017) Identification of dis-
crete low-temperature thermal events in polymetamorphic base-
ment rocks using high spatial resolution FE-SEM-EDX U-Th-Pb
dating of uraninite microcrystals. Geology 45:991–994. https://
doi.org/10.1130/G39370.1

Gaft M, Reisfeld R, Panczer G (2005) Modern luminescence spec-
troscopy of minerals and materials. Springer, Berlin; New York

Gaft M, Reisfeld R, Panczer G et al (1998) Laser-induced time-resolved
luminescence of minerals. Spectrochim Acta A Mol Biomol Spec-
trosc 54:2163–2175. https://doi.org/10.1016/S1386-1425(98)
00134-6

Ghaderi M, Palin JM, Campbell IH, Sylvester PJ (1999) Rare earth element systematics in scheelite from hydrothermal gold deposits in the Kalgoorlie-Norseman region, Western Australia. Econ Geol 94:423–437. https://doi.org/10.2113/gsecongeo.94.3.423

Gibert F, Moine B, Schott J, Dandurand J-L (1992) Modeling of the transport and deposition of tungsten in the scheelite-bearing calc-silicate gneisses of the Montagne Noire, France. Contrib Mineral Petrol 112:371–384. https://doi.org/10.1007/BF00310467

Harlov DE, Förster H-J (2004) Fluid-induced nucleation of (Y+REE)-phosphate minerals within apatite: Nature and experiment. Part II. Fluorapatite. Am Mineral 88:1209–1229. https://doi.org/10.2138/am-2003-8-905

Harlov DE, Wirth R, Förster H-J (2005) An experimental study of dissolution–reprecipitation in fluorapatite: fluid infiltration and the formation of monazite. Contrib Mineral Petrol 150:268–286. https://doi.org/10.1007/s00410-005-0017-8

Höck V (1993) The Habach-Formation and the Zentralgneis—a key in understanding the Palaeozoic evolution of the Tauern Window (Eastern Alps). In: Pre-Mesozoic geology in the Alps. Springer, pp 361–374

Höll R (1975) Die Scheelitlagerstätte Felbertal und der Vergleich mit anderen Scheelitvorkommen in den Ostalpen: A, Textteil. Verlag d. Bayer. Akademie d, Wiss

Höll R, Eichhorn R (1998) Tungsten mineralization and metamorphic remobilization in the Felbertal scheelite deposit, Central Alps, Austria. In: Metamorphic and Metamorphogenic Ore Deposits. Society of Economic Geologists

Höll R, Maucher A, Westenberger H (1972) Synsedimentary-diagenetic ore fabrics in the strata-and time-bound scheelite deposits of Kleinarltal and Felbertal in the Eastern Alps. Mineral Deposita 7:217–226

Höll R, Schenk P (1988) Metamorphosed hydrothermal eruption breccia (conglomerate) in the Felbertal scheelite deposit, Eastern Alps, Austria. Mar Geol 84:273–282

Hsu LC (1977) Effects of oxygen and sulfur fugacities on the scheelite-tungstenite and powellite-molybdenite stability relations. Econ Geol 72:664–670

Hsu LC, Galli PE (1973) Origin of the scheelite-powellite series of minerals. Econ Geol 68:681–696

Hulsbosch N, Boiron M-C, Dewaele S, Muchez P (2016) Fluid fractionation of tungsten during granite–pegmatite differentiation and the metal source of peribatholitic W quartz veins: Evidence from the Karagwe-Ankole Belt (Rwanda). Geochim Cosmochim Acta 175:299–318. https://doi.org/10.1016/j.gca.2015.11.020

Irber W (1999) The lanthanide tetrad effect and its correlation with K/Rb, Eu/Eu∗, Sr/Eu, Y/Ho, and Zr/Hf of evolving peraluminous granite suites. Geochim Cosmochim Acta 63:489–508. https://doi.org/10.1016/S0016-7037(99)00027-7

Jochum KP, Weis U, Stoll B et al (2011) Determination of Reference Values for NIST SRM 610-617 Glasses Following ISO Guidelines. Geostand Geoanal Res 35:397–429. https://doi.org/10.1111/j.1751-908X.2011.00120.x

Kazamel BG, Jamieson HE, Leybourne MI et al (2023) Aqueous Geochemistry and Mineralogy of Tungsten with Emphasis on Mine Wastes. Econ Geol 118:659–674. https://doi.org/10.5382/econgeo.4939

Kempe U, Trinkler M, Wolf D (1991) Yttrium und die Seltenerdfotolumineszenz natürlicher Scheelite. Chem Erde 51:275–289

Keppler H (1993) Influence of fluorine on the enrichment of high field strength trace elements in granitic rocks. Contrib Mineral Petrol 114:479–488. https://doi.org/10.1007/BF00321752

Kozlik M (2015) Mineralogical, petrological and (isotope-) geochemical studies on the Felbertal scheelite deposit, Austria: Development of an epigenetic model for W mineralization in the context of Variscan magmatism in the Tauern Window. PhD Thesis, University of Leoben

Kozlik M, Gerdes A, Raith JG (2016a) Strontium isotope systematics of scheelite and apatite from the Felbertal tungsten deposit, Austria – results of in-situ LA-MC-ICP-MS analysis. Mineral Petrol 110:11–27. https://doi.org/10.1007/s00710-015-0416-0

Kozlik M, Raith JG (2017) Variscan metagranitoids in the central Tauern Window (Eastern Alps, Austria) and their role in the formation of the Felbertal scheelite deposit. Lithos 278–281:303–320. https://doi.org/10.1016/j.lithos.2017.02.003

Kozlik M, Raith JG, Gerdes A (2016b) U–Pb, Lu–Hf and trace element characteristics of zircon from the Felbertal scheelite deposit (Austria): New constraints on timing and source of W mineralization. Chem Geol 421:112–126. https://doi.org/10.1016/j.chemgeo.2015.11.018

Krause J, Harlov DE, Pushkarev EV, Brügmann GE (2013) Apatite and clinopyroxene as tracers for metasomatic processes in nepheline clinopyroxenites of Uralian-Alaskan-type complexes in the Ural Mountains, Russian Federation. Geochim Cosmochim Acta 121:503–521. https://doi.org/10.1016/j.gca.2013.06.013

Lecumberri-Sanchez P, Vieira R, Heinrich CA et al (2017) Fluid-rock interaction is decisive for the formation of tungsten deposits. Geology 45:579–582. https://doi.org/10.1130/G38974.1

Leng C, Wang Y, Zhang X et al (2018) Constraints of molybdenite Re–Os and scheelite Sm–Nd ages on mineralization time of the Kukaazi Pb–Zn–Cu–W deposit, Western Kunlun, NW China. Acta Geochim 37:47–59. https://doi.org/10.1007/s11631-017-0205-z

Li B, Yang X, Wang X et al (2024) Genesis of tungsten mineralization in the Yangla copper-polymetallic deposit, northwest Yunnan, China: Evidence from in situ U-Pb dating, trace elements, Sr isotopes, fluid inclusions, and H-O isotopes of scheelite. Gondwana Res 129:167–192. https://doi.org/10.1016/j.gr.2023.12.008

Loges A, Migdisov AA, Wagner T et al (2013) An experimental study of the aqueous solubility and speciation of Y(III) fluoride at temperatures up to 250°C. Geochim Cosmochim Acta 123:403–415. https://doi.org/10.1016/j.gca.2013.07.031

Mao J, Ouyang H, Song S, et al (2019) Chapter 10 Geology and Metallogeny of Tungsten and Tin Deposits in China. In: Chang Z, Goldfarb RJ (eds) Mineral Deposits of China. Society of Economic Geologists, p 0

McDonough WF, Sun S -s. (1995) The composition of the Earth. Chem Geol 120:223–253. https://doi.org/10.1016/0009-2541(94)00140-4

Miranda ACR, Beaudoin G, Rottier B (2022) Scheelite chemistry from skarn systems: implications for ore-forming processes and mineral exploration. Mineral Deposita 57:1469–1497. https://doi.org/10.1007/s00126-022-01118-y

Nassau K (1963) Calcium tungstate—IV: the theory of coupled substitution. J Phys Chem Solids 24:1511–1517

Nassau K, Loiacono GM (1963) Calcium tungstate—III: Trivalent rare earth substitution. J Phys Chem Solids 24:1503–1510

Neuser RD, Bruhn F, Götze J et al (1995) Kathodolumineszenz: Methodik und Anwendung. Zentralblatt Für Geol Paläontol Teil H 1:287–306

Poulin RS, Kontak DJ, McDonald A, McCLenaghan MB (2018) Assessing Scheelite As an Ore-deposit Discriminator Using Its Trace-element and REE Chemistry. Can Mineral 56:265–302. https://doi.org/10.3749/canmin.1800005

Poulin RS, McDonald AM, Kontak DJ, McClenaghan MB (2016) On the Relationship Between Cathodoluminescence and the Chemical Composition of Scheelite From Geologically Diverse Ore-Deposit Environments. Can Mineral 54:1147–1173. https://doi.org/10.3749/canmin.1500023

Putnis A (2002) Mineral replacement reactions: from macroscopic observations to microscopic mechanisms. Mineral Mag 66:689–708. https://doi.org/10.1180/0026461026650056

Putnis A, Austrheim H (2010) Fluid-induced processes: metasomatism and metamorphism. Geofluids. https://doi.org/10.1111/j.1468-8123.2010.00285.x

Raimbault L, Baumer A, Dubru M et al (1993) REE fractionation between scheelite and apatite in hydrothermal conditions. Am Mineral 78:1275–1285

Raith J, Gerdes A, Cornell D (2011) In-situ U-Pb dating of scheelite: constraints on the age and genesis of the Felbertal tungsten deposit. In: Goldschmidt Conference Abstracts, p 1690

Raith J, Schmidt S, Aupers K (2018) Field Trip Pre-EX-5. Tungsten deposit Felbertal, Salzburg, Austria. In: XXI International Congress of the Carpathian Balkan Geological Association (CBGA 2018) Berichte der Geologischen Bundesanstalt. p 1

Raith JG, Stein HJ (2006) Variscan ore formation and metamorphism at the Felbertal scheelite deposit (Austria): constraining tungsten mineralisation from Re–Os dating of molybdenite. Contrib Mineral Petrol 152:505–521. https://doi.org/10.1007/s00410-006-0118-z

Rapp JF, Klemme S, Butler IB, Harley SL (2010) Extremely high solubility of rutile in chloride and fluoride-bearing metamorphic fluids: An experimental investigation. Geology 38:323–326. https://doi.org/10.1130/G30753.1

Schenk P (1990) Mikrothermometrische, gefügekundliche und geochemische Untersuchungen zur Genese der Scheelitlagerstätte Felbertal, Ostalpen. Inst. für Allg. u. Angewandte Geologie d. Ludwig-Maximilians-Univ.

Schenk P, Höll R (1991) Evolution of fluids and metamorphic ore remobilization in the Felbertal scheelite deposit, Eastern Alps. Ore Geol Rev 6:425–434

Schenk P, Höll R, Ivanova GF et al (1990) Fluid inclusion studies of the Felbertal scheelite deposit. Geol Rundsch 79:451–466

Schmid SM, Scharf A, Handy MR, Rosenberg CL (2013) The Tauern Window (Eastern Alps, Austria): a new tectonic map, with cross-sections and a tectonometamorphic synthesis. Swiss J Geosci 106:1–32. https://doi.org/10.1007/s00015-013-0123-y

Schmidt S (1988) Geologische Kartierung im Bereich der Scheelitlagerstätte Felbertal, Mittersill/Österreich. PhD Thesis

Sciuba M, Beaudoin G, Grzela D, Makvandi S (2020) Trace element composition of scheelite in orogenic gold deposits. Mineral Deposita 55:1149–1172. https://doi.org/10.1007/s00126-019-00913-4

Shatagin KN, Volkov VN (2020) Peculiarities of the Rb–Sr Isotope System in Granites: Comparative Study Results for Fresh and Altered Plagioclase Varieties from the Raumid Pluton Leucogranites (Pamirs). Dokl Earth Sci 493:604–607. https://doi.org/10.1134/S1028334X2008019X

Shore M, Fowler AD (1996) Oscillatory zoning in minerals; a common phenomenon. Can Mineral 34:1111–1126

Song G, Qin K, Li G et al (2014) Scheelite elemental and isotopic signatures: Implications for the genesis of skarn-type W-Mo deposits in the Chizhou Area, Anhui Province, Eastern China. Am Mineral 99:303–317. https://doi.org/10.2138/am.2014.4431

Stepanov A, A Mavrogenes J, Meffre S, Davidson P (2014) The key role of mica during igneous concentration of tantalum. Contrib Mineral Petrol 167:1009. https://doi.org/10.1007/s00410-014-1009-3

Stoll B, Jochum KP, Herwig K et al (2008) An Automated Iridium-Strip Heater for LA-ICP-MS Bulk Analysis of Geological Samples. Geostand Geoanal Res 32:5–26. https://doi.org/10.1111/j.1751-908X.2007.00871.x

Su Q, Mao J, Sun J et al (2020) Geochemistry and Origin of Scheelites from the Xiaoyao Tungsten Skarn Deposit in the Jiangnan Tungsten Belt, SE China. Minerals 10:271. https://doi.org/10.3390/min10030271

Thalhammer O (1987) Boninites as source rocks of tungsten mineralization at Mittersill, Austria? Mineral Petrol 37:221–242

U. S. Geological Survey (2022) Mineral commodity summaries 2022. U.S. Geological Survey, Reston, VA

Uspensky E, Brugger J, Graeser S (1998) REE geochemistry systematics of scheelite from the Alps using luminescence spectroscopy: from global regularities to local control. Schweiz Mineral Petrogr Mitt 78:31–54

von Quadt A (1993) The Saxonian Granulite Massif: new aspects from geochronological studies. Geol Rundsch 82:516–530

von Raumer JF, Bussy F, Schaltegger U et al (2013) Pre-Mesozoic Alpine basements—Their place in the European Paleozoic framework. Geol Soc Am Bull 125:89–108. https://doi.org/10.1130/B30654.1

Walker JB, Choppin GR (1967) Thermodynamic Parameters of Fluoride Complexes of the Lanthanides. Lanthanide/Actinide Chemistry. American Chemical Society, In, pp 127–140

Wood SA, Samson IM (2000) The Hydrothermal Geochemistry of Tungsten in Granitoid Environments: I. Relative Solubilities of Ferberite and Scheelite as a Function of T, P, pH, and mNaCl. Econ Geol 95:143–182. https://doi.org/10.2113/gsecongeo.95.1.143

Xiao X, Zhou T, Shi K et al (2022) Trace elements and textures of scheelite in porphyry-skarn Cu-Au systems: The example of Dongguashan deposit, eastern China. Ore Geol Rev 149:105069. https://doi.org/10.1016/j.oregeorev.2022.105069